

# Rotation Equivariant Proximal Operator for Deep Unfolding Methods in Image Restoration

Jiahong Fu, Qi Xie, Deyu Meng and Zongben Xu

**Abstract**—The deep unfolding approach has attracted significant attention in computer vision tasks, which well connects conventional image processing modeling manners with more recent deep learning techniques. Specifically, by establishing a direct correspondence between algorithm operators at each implementation step and network modules within each layer, one can rationally construct an almost “white box” network architecture with high interpretability. In this architecture, only the predefined component of the proximal operator, known as a proximal network, needs manual configuration, enabling the network to automatically extract intrinsic image priors in a data-driven manner. In current deep unfolding methods, such a proximal network is generally designed as a CNN architecture, whose necessity has been proven by a recent theory. That is, CNN structure substantially delivers the translational invariant image prior, which is the most universally possessed structural prior across various types of images. However, standard CNN-based proximal networks have essential limitations in capturing the rotation symmetry prior, another universal structural prior underlying general images. This leaves a large room for further performance improvement in deep unfolding approaches. To address this issue, this study makes efforts to suggest a high-accuracy rotation equivariant proximal network that effectively embeds rotation symmetry priors into the deep unfolding framework. Especially, we deduce, for the first time, the theoretical equivariant error for such a designed proximal network with arbitrary layers under arbitrary rotation degrees. This analysis should be the most refined theoretical conclusion for such error evaluation to date and is also indispensable for supporting the rationale behind such networks with intrinsic interpretability requirements. Through experimental validation on different vision tasks, including blind image super-resolution, medical image reconstruction, and image de-raining, the proposed method is validated to be capable of directly replacing the proximal network in current deep unfolding architecture and readily enhancing their state-of-the-art performance. This indicates its potential usability in general vision tasks. The code of our method is available at <https://github.com/jiahong-fu/Equivariant-Proximal-Operator>.

**Index Terms**—Proximal operator, deep unfolding network, rotation symmetry prior, image super-resolution, medical image reconstruction, image deraining.

## 1 INTRODUCTION

WITH the rapid development of deep learning (DL), convolutional neural network-based approaches have achieved great successes in the field of image restoration (IR). Among them, the deep unfolding approach finely integrates the advantages of conventional model-driven and current data-driven DL methodologies. This has recently attracted extensive research attention and achieved state-of-the-art (SOTA) performance over multiple IR tasks [1], [2], [3], [4], [5], e.g., blind image super-resolution [6], medical image reconstruction [7], and image de-raining [8].

The superiority of the deep unfolding approach mainly lies in its two specific characteristics. On one hand, it explicitly associates network modules in each layer with operators at each step of a carefully designed algorithm. This results in a deep unfolding network with an almost “white box” architecture, where only the priori solution part of the proximal operator is required to be manually pre-specified, resulting in a high degree of interpretability. This facilitates the network to easily embed helpful domain knowledge of a specific IR task, especially its underlying physical generalization mechanism, into its architecture construction. This then naturally makes the network better customized and more properly designed against the investigated task,

and achieves good performance in diverse image processing fields, like natural image restoration and medical imaging reconstruction [1], [2], [3], [4], [5].

On the other hand, the priori solution part of the proximal operator, as the main learning part of a deep unfolding network, facilitates the capability of the network to extract intrinsic image priors in a data-driven manner automatically. Specifically, it has been widely recognized that the performance of traditional model-driven methods heavily depends on meticulously pre-designed prior terms, with widely used priors such as sparsity, low-rankness and smoothness. However, manually crafting image priors is an invariably challenging endeavor, especially for real images with complex configurations. In contrast, the deep unfolding approach explores a way of learning image priors through a parameterized proximal operator (i.e., a proximal network) exclusively from data. This significantly enhances the model’s ability to represent image priors and thereby boosts its overall performance for general IR tasks.

As the most essential component, a proper design for such a proximal network always plays a critical role in the final effect of the deep unfolding methods. Currently, a series of proximal network forms have been attempted on different IR tasks, such as ResNet-based [9], [10], U-Net-based [11], [12], [13], and transformer-based [14] proximal networks. Actually, an interesting observation is that most studies lean to select certain CNN-based network structures to design such proximal network forms. The reasoning

Jiahong Fu, Qi Xie, Deyu Meng and Zongben Xu are with School of Mathematics and Statistics and Ministry of Education Key Lab of Intelligent Networks and Network Security, Xi’an Jiaotong University, Shaanxi, P.R.China.  
Email:jiahongfu@stu.xjtu.edu.cn, {xie.qi, dymeng, zbxu}@mail.xjtu.edu.cn

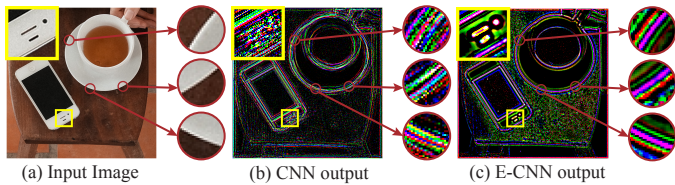


Fig. 1. Illustration of the output feature map of a typical image obtained by standard CNN and our used rotation equivariant convolution neural network (E-CNN).

behind this inclination and its necessity are illuminated by a recent theory expounded in [15]. That is, the CNN architecture can be proved to possess substantial a translation equivariance<sup>1</sup> property in theory, intrinsically delivering the translational symmetry image prior. This symmetry prior is universally present in general images, like natural, medical and remote sensing image domains. Succeeded from conventional prior terms, most of which are necessary with translational invariance property, CNN naturally becomes the most rational selection for setting proximal network in deep unfolding methodology.

The main value of the theory presented in [15] is that it provides a fundamental principle for purposefully designing proximal networks in deep unfolding implementations, i.e., embedding more meaningful and general transformation symmetry priors underlying the investigated IR task into the network. From this perspective, the currently used proximal networks still have evident limitations and performance improvement room. The most typical one is that current standard CNN-based proximal networks are limited in capturing the rotation symmetry prior, which yet should be another universal structural prior underlying general images besides translation symmetry. As intuitively demonstrated in Fig. 1(a), different image patches in an image can exhibit similar patterns, though they are in different orientations. Actually, rotation symmetry prior can be rationally embedded in the rotation invariance<sup>2</sup>. It is easy to deduce that most of the traditionally used regularization terms for reflecting image priors are invariant with respect to orientation, as well as translation. For example, rotating an image wouldn't theoretically change the values of the commonly used local smoothness, non-local self-similarity, low-rankness or other image prior terms. Fig. 2 demonstrates this regularizer property in general, where one can easily observe that the values of Lap  $L_0$  [16],  $L_1$  [17], TV and second-order TV norms [18] of the same image only vary slightly when the image is rotated<sup>3</sup>. According to the principle provided in [15], this implies that orientation equivariance of the proximal network for IR tasks should also be necessarily desired, which yet not hold for current

<sup>1</sup>Translation equivariance means that shifting an input image of CNN is equivalent to shifting all of its intermediate feature maps and output image, and translation invariance means that shifting an input image of CNN does not change its intermediate feature maps and output image.

<sup>2</sup>Rotation invariance means that rotating the input image of an operator will not change the output.

<sup>3</sup>Their mild intensity variations are conducted by discretization error of image representation. More dataset statistics can be found in the supplementary material.

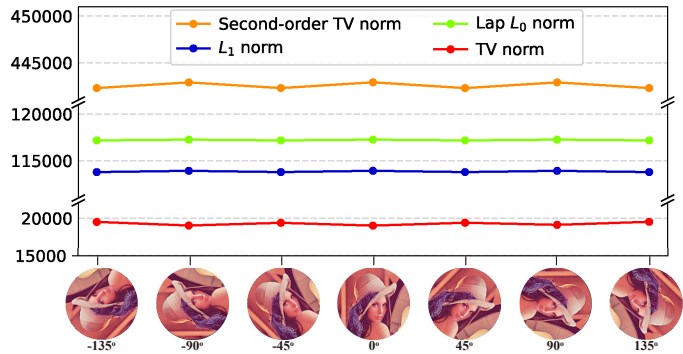


Fig. 2. The values of four typical conventional regularization terms on the Lena image with different rotation angles.

mainstream CNNs, as clearly shown in Fig. 1(b).

In this study, we devote to exploiting rotation equivariant convolution network and theory, aiming to make it capable of being properly equipped on proximal network design for general IR tasks. The method is expected to be both easily operated in practice and strictly supported in theory, where the latter is especially important and indispensable for the deep unfolding methodology that has inherent interpretability requirement.

Specifically, the main contribution of this paper can be mainly summarized as follows:

1) We suggest a high-accuracy rotation equivariant proximal network for deep unfolding methods through comprehensive attempts and evaluations. By easily replacing the convolutions in current proximal networks with such rotation equivariant amelioration, the rotational symmetry image prior can be readily embedded into the deep unfolding network, and also help make the network more lightweight by allowing convolutions able to share representations for more essentially similar local structures.

2) We provide thorough theoretical equivariant error analysis for the suggested rotation equivariant proximal network with arbitrary layers under arbitrary rotation degrees, which strictly reveals how the selected rotation group's cardinality for equivariant convolutions and the image resolution influence the equivariant error. To the best of our knowledge, this should be the most refined theoretical conclusion for such error evaluation to date, and thus meaningful for general deep unfolding network design.

3) By readily replacing the proximal components within current deep unfolding networks with the suggested rotation equivariant ones for different IR tasks, including blind image super-resolution, medical image reconstruction and image deraining, we have substantiated that such amelioration facilitates the model able to consistently surpass the performance of SOTA methods designed for these tasks and also exhibit superior generalization capabilities. This indicates the potential applicability of this method across more general deep unfolding techniques.

The remainder of this paper is organized as follows. Section 2 provides an overview of related works and introduces the concept of equivariant prior knowledge and definitions. Section 3 presents the suggested equivariant proximal operator network with its error analysis theory. Section 4 demonstrates experiments on evaluating the performance of

the method on general IR tasks. The paper finally concludes with a future work discussion.

## 2 RELATED WORK

### 2.1 Deep Unfolding Network for Image Restoration

Deep unfolding methods can be mainly categorized into deep Plug-and-Play (PnP) and deep unrolling methods, which have been widely used for various IR tasks.

The early PnP algorithms can be traced back to [19], [20], [21], [22], [23]. By replacing the proximal operator in Alternating Direction Method of Multipliers (ADMM) with off-the-shelf denoisers (e.g., BM3D [24] or Total Variation [18]), Venkatakrisnan et al. [22] proposed the concept of PnP priors. These innovative approaches inspire researchers to replace the explicit prior of model-based methods with an implicit prior of denoiser for PnP methods. Such advantages lay the foundation for leveraging deep CNN denoisers to improve effectiveness. Recently, deep PnP methods [12], [25], [26], [27] have achieved good progress across multiple tasks by introducing a learnable denoiser with deep learning. These works [12], [28], [29], [30] have applications such as denoising, deblurring, super-resolution, inpainting, and medical imaging. Compared with PnP, which requires a manually specified denoiser, deep PnP inclines to learn a more accurate data-related denoiser prior through a deep neural network, which not only shortens the steps of the algorithm but also achieves better performance.

To leverage domain knowledge and observation model for image restoration, deep unrolling methods aim to replace certain steps in an algorithm with learnable parameters [3], [31], [32]. Inspired by LISTA [31], Wang et al. [33] designed a deep unrolling method for image super-resolution based on sparse coding. In [4], Yang et al. proposed ADMM-Net, which is derived from the iterative procedures in alternating direction method of multipliers algorithm for optimizing a compressive-sensing-based magnetic resonance imaging (MRI) model. Since then, a series of deep unfolding methods based on specific optimization algorithms have been applied to various IR tasks. Such algorithm unfolding attempts include first-order-gradient-based unfolding networks [4], [26], [34], [35], [36], [37], second-order-gradient-based unfolding network [38], [39] and Half-Quadratic-Splitting algorithm based unfolding method [5], [12], [40] and so on. Typically, there is a class of Iterative Shrinkage-Thresholding Algorithms (ISTA) [41], [42], which is usually with simple iterative formulations for IR tasks, and has been shown to be suitable for designing deep unfolding networks [8], [10], [43], [44].

In the aforementioned algorithms (e.g. AMDD, HQS, and ISTA), the proximal operator usually plays an important role. Intrinsically, such proximal operator is related to the pre-specified prior terms, e.g., the  $L_1$ -norm term, representing the sparsity prior, corresponds to a soft-thresholding operator. Thus, proximal network design is the key issue in constructing unfolding networks. The most intuitive way [31], [45] for proximal operator design is to set scalars/matrices *etc.* in iterative algorithms as learnable parameters and learn them by data-driven training. These methods usually need to manually assume a prior for the

correlated tasks, and then deduce the formulation of the corresponding thresholding operator before training. To release the difficulty and inaccuracy in manually designing image prior, more latest researchers attempt to further parameterize the proximal operator as a pure deep neural network, i.e., proximal network, based on Convolution+BN+ReLU [46], Encoder-Decoder structure [5], [26], ResNet structure [8], [10], [47] and so on. Recently, transformer-based proximal networks have also received attention [14].

The key drawback of these data-dependent proximal network attempts is that most of them are heuristically constructed with existing deep network architectures, while rarely evaluating their underlying construction mechanism on how they could insightfully embed intrinsic image priors. This research focuses on the most typical issue along this research line, i.e., how to embed rotation symmetry prior, one of the most universal priors underlying general images, into a proximal network to enhance the capability of deep unfolding in an implementable easy and theoretically sound manner.

### 2.2 Group Equivariant CNNs

A series of recent works have been proposed to incorporate equivariance into networks, for modeling the transform symmetry priors existing in data samples, such as translation, rotation, scaling and reflection symmetries. Formally, let  $\Psi$  be a mapping from the input feature space to the output feature space, and  $G$  be a group of transformations. We say  $\Psi$  is group equivariance about  $G$ , if for any  $g \in G$ ,

$$\Psi [\pi_g[X]] = \pi'_g [\Psi[X]] \quad (1)$$

where  $X$  represents an input image or a feature map, and  $\pi_g$  and  $\pi'_g$  denote how the transformation  $g$  acts on input and output features, respectively.

Multiple pieces of literature have begun to investigate how to explicitly incorporate transformation equivariance into neural network architectures. Specifically, G-CNN [48] and HexaConv [49] explicitly integrate  $\pi/2$  and  $\pi/3$  degree rotation equivariances into the neural network, respectively. Subsequently, a more comprehensive equivariance is achieved based on interpolation [50], [51] and Gaussian-resampling [52] technology. Very recently, the filter parametrization technique has been employed for designing G-CNNs. Early attempts [53], [54] were made to use harmonics as steerable filters to achieve exact equivariance with respect to larger transformation groups in the continuous domain. After that, [55] and [56] designed equivariance by relating convolution with partial differential operators and proposed PDO-eConv. However, these methods still suffer from low expression accuracy problems in filter parametrization methods, which results in their inferior performance in IR tasks. Very recently, Xie et al. [57] proposed Fourier series expansion-based filter parametrization, which has relatively high expression accuracy. They further constructed F-Conv, an equivariant convolution method suitable for IR tasks, and it has been verified to be effective.

The main issue of current rotation equivariant convolution research should be on their theoretical level, which can only provide equivariant error support on limited discrete orientation degrees on one single network layer. This issue

is particularly critical for deep unfolding context since this methodology places a specific emphasis on network interpretability. Therefore, it particularly expects a clear theoretical error evaluation to support the rationale of embedding rotation equivariance into multi-layer proximal networks repetitively appearing throughout the deep unfolding network. This is also the main focus of this study, i.e., ensuring that the implementation of rotation equivariant embedding is not only heuristic but also provides valuable scientific inspiration for future research.

### 3 EQUIVARIANT PROXIMAL NETWORK

#### 3.1 General Framework of Deep Unfolding

For a general image restoration task, the underlying high-quality image  $X$  is expected to be restored from its degraded measurement  $Y$ . Formally, the correlated ill-posed inverse problem can be formulated as following [58]:

$$\min_X L(X, Y) + \lambda R(X), \quad (2)$$

where  $\lambda$  denotes the trade-off parameter;  $L(X, Y)$  is the data fidelity term, which is often set as  $L(X, Y) = \|Y - AX\|_F^2$ ; and  $R(X)$  is the regularization term. It should be noted that in traditional model-based IR methods, the design of  $R(X)$  plays the most substantial role in image prior modeling and significantly influences application performance. Correspondingly, designing  $R(X)$  is also one of the most challenging tasks in IR method formulations.

There are multiple ways for solving Eq. (2). In this paper, we mainly consider the ISTA algorithm [41], [42], which should be one of the most popular choices for addressing general IR tasks. Generally, in the ISTA algorithm, the following quadratic approximation of (2) is iteratively solved:

$$\min_X L(X^{(t)}, Y) + \langle \nabla L(X^{(t)}, Y), X - X^{(t)} \rangle + \frac{1}{2\eta} \|X - X^{(t)}\|_F^2 + \lambda R(X), \quad (3)$$

where  $X^{(t)}$  denotes the updating result after the  $t^{\text{th}}$  iteration. After organizing and simplifying the updating equation, we can obtain the following update process:

$$X^{(t+1)} = \arg \min_X \frac{1}{2} \|X - \tilde{X}^{(t)}\|_F^2 + \eta \lambda \mathcal{R}(X), \quad (4)$$

where  $\tilde{X}^{(t)} = X^{(t)} - \eta \nabla h(X^{(t)})$  and  $\eta$  denotes the step-size parameter.

Solving the regularized minimization problem (4) is the key progress of the algorithm. Usually, the following closed-form solutions can be deduced [59]:

$$X^{(t+1)} = \text{prox}_R(\tilde{X}^{(t)}) = \text{prox}_R(X^{(t)} - \eta \nabla h(X^{(t)})), \quad (5)$$

where  $\text{prox}_R(\cdot)$  is the proximal operator [60] corresponding to  $R(\cdot)$ . It is easy to find that the image prior knowledge is indeed mainly reflected in  $\text{prox}_R(\cdot)$  when solving the problem. This inspires the construction of deep unfolding networks, aiming to directly encode image prior in its proximal network modules. This approach eliminates the need for the manual design of regularization terms and solving of the regularized minimization problem (4), simultaneously.

In the past years, several deep-learning-based proximal networks have been constructed to characterize such data-dependent priors [4] [12] [10], which well employs such a data-driven prior learning manner and achieved good performance across various IR tasks.

#### 3.2 A Principle for Proximal Network Design

As aforementioned, the performance of a deep unfolding method highly relies on the rational design of the proximal network, which plays an implicit role in incorporating crucial image prior knowledge into the network and thus facilitating easy training and good generalization of the entire network. Most of the existing deep unfolding methods tend to use multi-layer CNNs/ResNet to specify this proximal network [4], [10], [12], but less considering why this architecture is necessary and how to further incorporate more important image priors into it.

Very Recently, Celledoni et al. [15] conducted a meaningful exploration against this issue, and revealed a principle for such proximal network  $\text{prox}_R(\cdot)$  design. Specifically, it is theoretically proved that when  $R(\cdot)$  is invariant to certain transformations like translation or rotation, then the proximal operator must be equivariant to the transformation. Formally, regarding an image as an element in a Hilbert space, the following lemma holds [15].

**Lemma 1.** *Suppose that  $\mathcal{X}$  is a Hilbert space and  $\pi_g : \mathcal{X} \rightarrow \mathcal{X}$  is an unitary transformation on  $\mathcal{X}$ . If a functional  $R : \mathcal{X} \rightarrow \mathbb{R} \cup \{+\infty\}$  is invariant, i.e.  $R(\pi_g(X)) = R(X)$ ,  $\forall X \in \mathcal{X}$ , and has a well-defined single-valued proximal operator  $\text{prox}_R : \mathcal{X} \rightarrow \mathcal{X}$ , then  $\text{prox}_R$  is equivariant, in the sense that*

$$\text{prox}_R[\pi_g](X) = \pi_g[\text{prox}_R](X), \forall X \in \mathcal{X}. \quad (6)$$

According to Lemma 1, it can be deduced that a key principle in designing a rational proximal network is to ensure its equivariance to certain unitary transformations when the regularization term for the target image is invariant under these transformations.

This conclusion actually explains why convolution-based proximal networks (such as CNNs and ResNets) are effective. Specifically, since images usually exhibit evident *translation symmetry*, it is easy to find that most conventional regularization terms designed for image data are with strict translation invariant property, i.e.,  $R[\pi_t](X) = R(X)$ . Moreover,  $\pi_t$  is indeed a unitary transformation<sup>4</sup>. This satisfies the condition of Lemma 1. Therefore, according to Celledoni's theory, translation equivariance is necessary for ISTA algorithms and their corresponding deep unfolding networks. As the most typical translation equivariant operator [61], the convolution structure naturally becomes a rational choice for setting proximal networks.

#### 3.3 Rotation Equivariant Proximal Network

Besides translation symmetry, rotation symmetry should also be considered as a universal structural prior underlying general images. As shown in Fig. 2, it is evident that the relative rotation invariant errors of typical commonly used

<sup>4</sup>Translation of a digital image  $X$  can be performed by changing the positions of elements of  $X$ , while changing element positions is a unitary transformation.

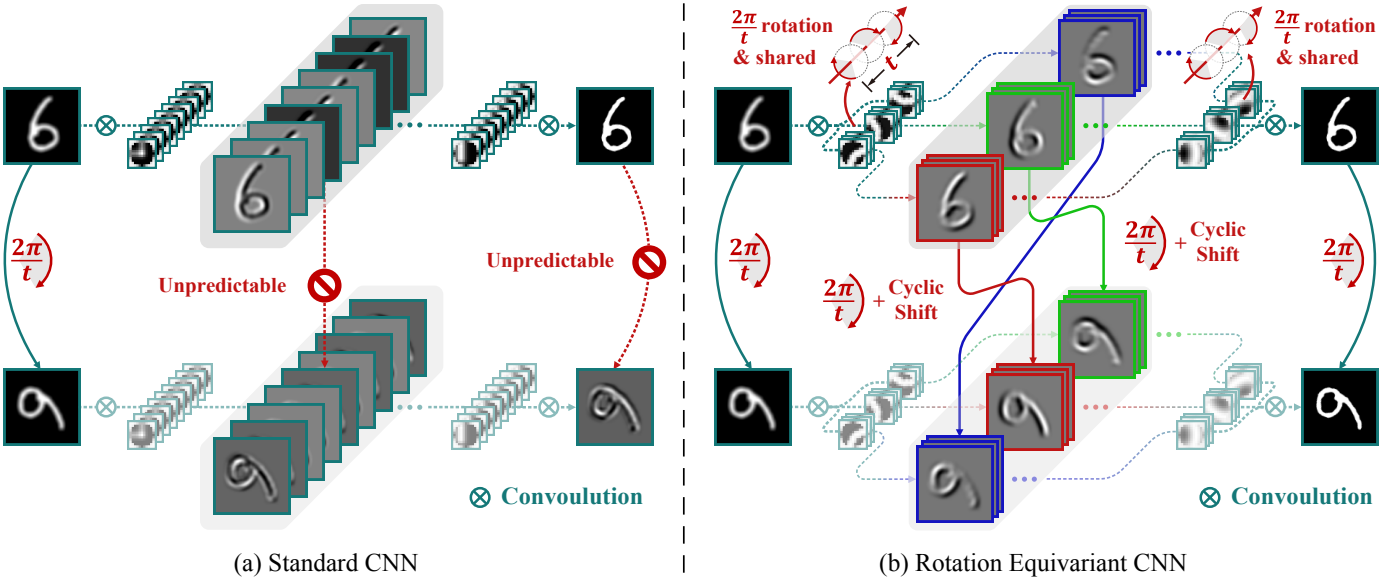


Fig. 3. Illustrations of the feature maps and outputs of different CNNs when rotating the input images for  $2k\pi/t$ , where  $k = 1, 2, \dots, t$ ,  $t$  is the equivariant number. (a) A standard CNN. (b) The rotation equivariant CNN with the same backbone.

regularization terms are consistently small. This implies that conventional regularization terms always have essentially embedded such important rotation invariance knowledge inside, also validating the universality of this specific image invariance prior. Consequently, this inspires us to necessarily design a rotation equivariant proximal network for deep unfolding networks based on Lemma 1.

It should be noted that most of the current proximal networks can indeed not be proved to be rotation equivariant. As shown in Fig. 3(a), in a standard convolutional network, when the input image is rotated, the relationship between feature maps before and after rotating the input image is intrinsically unpredictable. Fortunately, multiple rotation equivariant convolutions have been proposed in the past years, including GCNN [48], E2-CNN [54], PDO-eConv [55] and F-Conv [57]. These rotation equivariant convolutions demonstrate the potential for constructing a rotation equivariant proximal network for IR tasks.

Specifically, by replacing all convolutions in the CNN-based proximal networks with rotation equivariant ones, we can obtain rotation equivariant proximal networks without changing other architectures of the backbone, as shown in Fig. 3. For a network based on equivariant convolutions, when the input image is rotated by  $2k\pi/t$  degrees ( $k = 1, 2, \dots, t$ , where  $t$  is the equivariant number of the equivariant convolutions, as intuitively depicted in Fig. 3 (b) for easy understanding), then the change of all the feature maps are predictable. This change results from the combination of rotation and cyclic shifts in channels, and the output of the network is also rotated for  $2k\pi/t$  degree. One can view Fig. 3 to easily understand this progress.

Besides, by embedding such rotation equivariance to the CNN proximal network, the network is possibly expected to be more lightweight than commonly used CNNs. From Fig. 3 (a) and (b), one can easily see that the convolution filters in rotation equivariant convolutions have been rotated for  $\frac{2k\pi}{t}$ ,  $k = 1, 2, \dots, t$  degrees before performing

convolution operator, which means that all parameters for parameterized filters are reused  $t$  times. Therefore, when using the same number of channels, the rotation equivariant convolution only requires  $1/t$  convolution filters and thus tends to have fewer network parameters. This inclination to make the network parameters more efficiently used also hopefully leads to better generalization capabilities.

Now, we need to discuss two critical issues to guarantee a sound construction and utilization of such an expected rotation equivariant proximal network in general deep unfolding frameworks. The first is to suggest a proper equivariant convolution representation for implementing the intended task, and the second more important issue is to provide theoretical support to the suggested implementation manner. Specifically, the current analysis about equivariant error is only on one single convolution layer and with respect to finite discrete rotation degrees  $\theta = 2k\pi/t$  ( $k = 1, 2, \dots, t$ ). However, the interpretation requirement of deep unfolding methodology calls for the theoretical representation error support in proximal networks at arbitrary angles and multi-layer convolution networks.

### 3.4 Selection of Equivariant Convolutions

In previous pieces of literature [10], [11], [12], the proximal network is always regarded as an image denoiser for the solver of Eq. (4). It can be similarly seen as a denoising model. To evaluate the necessity of rotation equivariance for the proximal network and select a proper equivariant convolution for general IR tasks, we have carefully designed simulation denoising experiments for this purpose.

Specifically, the competing methods include standard CNN, Swin-Conv UNet (SCUNet) [14] and four SOTA equivariant convolution ameliorations, G-CNN [48], E2-CNN [53], PDO-eConv [55] and F-Conv [57]. We exploit the same backbone network for competing convolution methods, i.e., a ResNet [9] containing 16 residual blocks of 256

TABLE 1  
Average PSNR/SSIM of different competing methods on synthesized testing datasets.

Method	Urban100 [62]		BSD100 [63]		Set14 [64]		Set5 [65]	
	PSNR	SSIM	PSNR	SSIM	PSNR	SSIM	PSNR	SSIM
ProxCNN	30.57	0.8877	29.56	0.8171	29.86	0.8112	31.84	0.8807
ProxSCUNet	30.50	0.8887	29.55	0.8176	29.96	<b>0.8159</b>	31.79	0.8805
ProxG-CNN	30.75	0.8914	29.60	0.8199	29.89	0.8111	31.91	0.8825
ProxE2-CNN	30.66	0.8891	29.58	0.8177	29.79	0.8086	31.90	0.8817
ProxPDO-eConv	29.55	0.8628	29.19	0.7998	29.50	0.8030	31.47	0.8703
ProxF-Conv	<b>31.05</b>	<b>0.8962</b>	<b>29.66</b>	<b>0.8211</b>	<b>30.02</b>	0.8134	<b>31.98</b>	<b>0.8836</b>

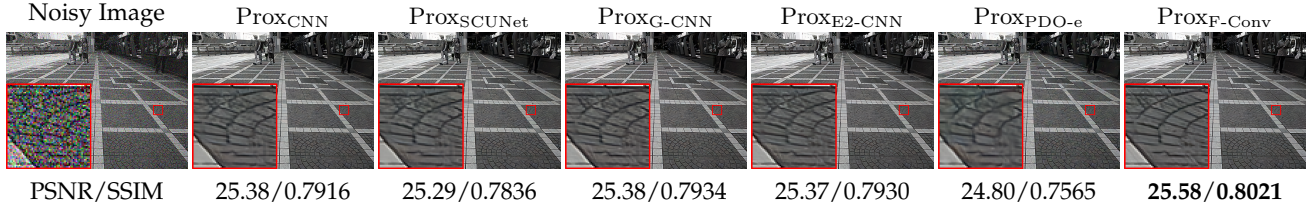


Fig. 4. Performance comparison *img 095* in Urban100 [62], where the Gaussian noise is with standard deviation of 50.

channels. We simulate Gaussian noise and train the proximal networks for denoising. All the competing methods use a filter size of  $5 \times 5$ . We set the equivariant number to  $t = 4$  for G-CNN since it is designed with  $t = 4$  and set  $t = 8$  for the other equivariant convolutions. All methods are trained with 800 samples from the DIV2K dataset [66], and the simulated Gaussian noise has a standard deviation of 50. Four well-known benchmark image datasets, including Set5 [65], Set14 [64], BSD100 [63], and Urban100 [62], are selected as testing datasets for our experiments.

As demonstrated in Table 1, the F-Conv based method exhibits clear superiority in performance when compared to the standard convolution (ProxCNN) and swin transformer based network (ProxSCUNet). This superiority can be attributed to the explicit representation of the rotation symmetry prior and the representation accuracy of the filter parametrization in F-Conv based convolutions. For the E2-CNN and PDO-eConv methods, although the rotation symmetry prior has also been represented, their performances do not exhibit significant advantages over standard CNN-based methods. This should be due to the limitation of representation accuracy of their filter parameterizations. Moreover, we provide visual denoising results in Fig. 4, and it is seen that F-Conv based proximal network inclines to restore the rotation-invariant structure better than others. These results inspire us to suggest F-Conv as the main tool to construct our rotation equivariant proximal network for deep unfolding against general IR tasks.

### 3.5 Theoretical Analysis for Equivariant CNN

It has been well proved that current equivariant convolutions are exact in the continuous domain. However, they would become approximate after necessary discretization for real-world applications [48], [54], [55], [57]. In the case of discretization, the latest theoretical analysis has derived the equivariant error specifically for  $t$  selected orientations within a single convolution layer, stated as follows [57]:

**Lemma 2.** For a one-layer equivariant convolution operation  $\text{Conv}_{eq}(\cdot)$  with  $t$  being its equivariant number, and an input image (or a feature map)  $X$ , under proper conditions, the following result holds:

$$|\text{Conv}_{eq}[\pi_\theta](X) - \pi_\theta[\text{Conv}_{eq}](X)| \leq C(p+1)^2 h^2, \quad (7)$$

$$\forall \theta = 2k\pi/t, k = 1, 2, \dots, t,$$

where  $\pi_\theta$  defines the rotation transformation of the input image (or on a feature map<sup>5</sup>),  $h$  is the mesh size,  $p$  is the filter size and  $C$  is a positive constant independent of  $h, p$ .

The left of (7) represents the equivariant error, i.e., the difference between the results obtained with rotation before and after convolutions. Lemma 2 shows that the equivariant error for a single-layer convolution would approach zero as the mesh size  $h$  approaches zero when the rotation degree is within the selected discrete set. This is consistent with human intuition because the equivariant error is caused by discretization, and an error caused by discretization approaches zero as the mesh size approaches zero.

However, it is important to understand how to evaluate the equivariant error for the entire equivariant network under arbitrary rotation degrees. When the rotation angle does not belong to the discrete rotation set or the equivariant convolution involves multiple layers, Lemma 2 can not be used to analyze the equivariant error correspondingly. Specifically, if the input image is rotated by  $\theta \neq 2k\pi/t$ , then the change of feature maps at each layer becomes unpredictable. This unpredictability arises because the cyclic shift of channels can only be performed for finite rotation angles  $\theta = 2k\pi/t, k = 1, 2, \dots, t$ . Therefore, the current theoretical analysis framework is no longer applicable for such purposes.

In order to deal with this issue, we deduce the following theorem for more comprehensively and accurately evaluating the rotation equivariant error.

<sup>5</sup>When  $\pi_\theta$  is the transformation on a feature map, it is combined of  $\theta$  degree rotation and  $k$  cyclic shift on the channels of the feature map. Please see more details in the supplementary material.

**Theorem 1.** For an image  $X$  with size  $H \times W \times n_0$ , and a  $N$ -layer rotation equivariant CNN network  $\text{CNN}_{eq}(\cdot)$ , whose channel number of the  $i^{\text{th}}$  layer is  $n_i$ , rotation equivariant subgroup is  $S \leq O(2)$ ,  $|S| = t$ , and activation function is set as ReLU. If the latent continuous function of the  $c^{\text{th}}$  channel of  $X$  denoted as  $r_c : \mathbb{R}^2 \rightarrow \mathbb{R}$ , and the latent continuous function of any convolution filters in the  $i^{\text{th}}$  layer denoted as  $\varphi^i : \mathbb{R}^2 \rightarrow \mathbb{R}$ , where  $i \in \{1, \dots, N\}$ ,  $c \in \{1, \dots, n_0\}$ , for any  $x \in \mathbb{R}^2$ , the following conditions are satisfied:

$$\begin{aligned} |r_c(x)| &\leq F_0, \|\nabla r_c(x)\| \leq G_0, \|\nabla^2 r_c(x)\| \leq H_0, \\ |\varphi^i(x)| &\leq F_i, \|\nabla \varphi^i(x)\| \leq G_i, \|\nabla^2 \varphi^i(x)\| \leq H_i, \\ \forall \|x\| &\geq (p+1)h/2, \varphi_i(x) = 0, \end{aligned} \quad (8)$$

where  $p$  is the filter size,  $h$  is the mesh size, and  $\nabla$  and  $\nabla^2$  denote the operators of gradient and Hessian matrix, respectively. For an arbitrary  $0 \leq \theta \leq 2\pi$ ,  $A_\theta$  denotes the rotation matrix, the following result is satisfied:

$$|\text{CNN}_{eq}[\pi_\theta](X) - \pi_\theta[\text{CNN}_{eq}](X)| \leq C_1 h^2 + C_2 p h t^{-1}, \quad (9)$$

where

$$\begin{aligned} C_1 &= 2N\mathcal{F} \cdot \sum_i \left( \mathcal{H}_i F_0 + 2\mathcal{G}_i \sum_{m=1}^{i-1} \mathcal{G}_m F_0 + 2\mathcal{G}_i G_0 + H_0 \right), \\ C_2 &= 2\pi G_0 \mathcal{F} (2 \max\{H, W\} p^{-1} + 2N), \\ \mathcal{F}_i &= n_{i-1} p^2 F_i, \mathcal{F} = \prod_i \mathcal{F}_i, \\ \mathcal{G}_i &= n_{i-1} p^2 G_i \text{ and } \mathcal{H}_i = n_{i-1} p^2 H_i. \end{aligned} \quad (10)$$

It should be indicated that to the best of our knowledge, Theorem 1 should firstly provide the bound of the equivariant error in relation to the multi-layer network under arbitrary rotation degrees<sup>6</sup>. It reveals that the equivariant error is primarily influenced by two factors: the mesh size ( $h$ ) and the equivariant number ( $t$ ). Consistent with Lemma 2, the equivariant error in Theorem 1 will become larger when the mesh size  $h$  increases. Besides, we can further achieve more insightful conclusions from this theoretical conclusion as follows:

(I) When the range of a convolution kernel is a constant, then  $ph$  remains constant. In this scenario, it becomes evident that the second term of the equivariant error bound primarily depends on  $t$ , and a larger  $t$  results in a smaller equivariant error. This fully complies with the intuition that designing equivariant convolution to be equivariant to more selected degrees reduces the equivariant error under arbitrary degrees.

(II) Interestingly, when  $t = 1$ , the network degenerates to a conventional CNN, and the equivariant convolution will not be equivariant anymore. This occurs because the second term in the error bound becomes a constant, and the error bound will never approach zero. This reveals why conventional CNNs do not possess intrinsic rotation equivariance properly.

Table 2 shows the mean rotation equivariant error ( $\|f[\pi_\theta](X) - \pi_\theta[f](X)\|_2 / \|f(X)\|_2$ ,  $\theta \sim U(-\pi, \pi)$ ) on a typical benchmark image dataset DIV2K [66]. We can clearly see that as the equivariant number increases, the equivariant error of the rotation equivariant convolution decreases

<sup>6</sup>One can refer to the supplementary material for the details of the proof.

TABLE 2

The rotation equivariant error,  $\|f[\pi_\theta](X) - \pi_\theta[f](X)\|_2 / \|f(X)\|_2$ , averaged over 10 random selected  $\theta$  and 100 random selected images on the dataset DIV2K [66].

CNN	Rotation Equivariant CNN					
	$t = 1$	$t = 2$	$t = 4$	$t = 8$	$t = 12$	$t = 24$
0.851	0.852	0.648	0.428	0.259	0.175	0.068

rapidly. When  $t = 1$  the equivariant error is similar to that of the ordinary CNN. The measure of equivariant error here is the relative calculation error. These results verify our aforementioned theoretical conjectures.

(III) Moreover, it is interesting to note that a component,  $n_{i-1} p^2$  (contained in all fundamental terms of  $\mathcal{F}_i$ ,  $\mathcal{G}_i$  and  $\mathcal{H}_i$ ), consistently emerges in both  $C_1$  and  $C_2$ . This observation fully accords with some well-known initialization schemes for convolution networks, such as Xavier initialization [67] and He's initialization [68].

In these initialization schemes, the elements of convolution kernels, denoted as  $v_\varphi^i$  at the  $i^{\text{th}}$  layer, are recommended to be initialized by sampling from Gaussian distribution  $N(0, \frac{c}{n_{i-1} p^2})$  or Uniform distribution  $U(-\frac{c}{n_{i-1} p^2}, \frac{c}{n_{i-1} p^2})$ , where  $c$  is a constant number. In other words,  $n_{i-1} p^2 v_\varphi^i \sim N(0, c)$  or  $U(-c, c)$ , which is rational to be assumed to be bounded with high probability. From this perspective, it should be rational to consider  $\mathcal{F}_i$ ,  $\mathcal{G}_i$ ,  $\mathcal{H}_i$  as bounded combined with the smoothness of the kernel.

In summary, it can be found that all conditions of Theorem 1 are easy to be satisfied in practice, which only need the first and second derivatives of the underlying function of the input image and convolution kernels to be bounded. As a result, This implies that the rotation equivariance of the suggested proximal network can be theoretically guaranteed for arbitrary rotation degrees and multiple network layers, under controllable rotation equivariant error in practice. Consequently, this enables deep unfolding networks equipped with such rotational equivariance proximal network to have solid theoretical guarantees and to maintain their substantial requirements for interpretability.

## 4 EXPERIMENTAL RESULTS

### 4.1 Blind Single Image Super-Resolution

We first test the effectiveness of the equivariant proximal work using the blind image super-resolution task. For image super-resolution, the main goal is to reconstruct the high-resolution image with high visual quality from an observed low-resolution image. The degradation model for blind super-resolution with a uniform kernel is commonly expressed as:

$$Y = (X \otimes K) \downarrow_s + N, \quad (11)$$

where  $X$  is the to-be-estimated high-resolution image,  $K$  is the blur kernel,  $\otimes$  denotes two-dimensional (2D) convolution operation,  $\downarrow_s$  represents the standard  $s$ -fold downsampler, *i.e.*, only keeping the upper-left pixel for each distinct  $s \times s$  patch [5], and  $N$  denotes the Additive White Gaussian Noise (AWGN).

TABLE 3  
Average PSNR/SSIM of the super-resolution results obtained by all comparison methods on different benchmark datasets.

Method	Scale	Urban100 [62]		BSD100 [63]		Set14 [64]		Set5 [65]		Standard
		PSNR	SSIM	PSNR	SSIM	PSNR	SSIM	PSNR	SSIM	Deviation
Bicubic	x2	23.00	0.6656	25.85	0.6769	25.74	0.7085	27.68	0.8047	0
RCAN [69]		23.22	0.6791	26.03	0.6896	25.92	0.7217	27.85	0.8095	
IKC [70]		27.46	0.8401	29.85	0.8390	30.69	0.8614	33.99	0.9229	
DASR [71]		26.65	0.8106	28.84	0.7965	29.44	0.8224	32.50	0.8961	
DAN [72]		27.93	0.8497	30.09	0.8410	31.03	0.8647	34.40	0.9291	
KXNet [6]		28.51	0.8667	30.38	0.8485	31.28	0.8697	35.00	0.9335	
KXNet-E <sub>X</sub>	<b>28.91</b>	<b>0.8758</b>	<b>30.63</b>	<b>0.8564</b>	<b>31.64</b>	<b>0.8756</b>	<b>35.21</b>	<b>0.9362</b>		
Bicubic	x3	21.80	0.6084	24.68	0.6254	24.28	0.6546	25.78	0.7555	0
RCAN [69]		21.38	0.6042	24.47	0.6299	24.07	0.6606	25.63	0.7572	
IKC [70]		25.36	0.7626	27.56	0.7475	28.19	0.7805	31.60	0.8853	
DASR [71]		25.20	0.7575	27.39	0.7379	27.96	0.7727	30.91	0.8723	
DAN [72]		25.82	0.7855	27.88	0.7603	28.69	0.7969	31.70	0.8940	
KXNet [6]		26.48	0.8056	28.26	0.7699	29.20	0.8066	32.82	0.9049	
KXNet-E <sub>X</sub>	<b>26.66</b>	<b>0.8128</b>	<b>28.34</b>	<b>0.7742</b>	<b>29.29</b>	<b>0.8096</b>	<b>32.95</b>	<b>0.9070</b>		
Bicubic	x4	20.88	0.5602	23.75	0.5827	23.17	0.6082	24.35	0.7086	0
RCAN [69]		19.84	0.5307	23.10	0.5729	22.38	0.5967	23.72	0.6973	
IKC [70]		24.33	0.7241	26.49	0.6968	27.04	0.7398	29.60	0.8503	
DASR [71]		24.20	0.7150	26.43	0.6903	26.89	0.7306	29.53	0.8455	
DAN [72]		24.91	0.7491	26.92	0.7168	27.69	0.7600	30.53	0.8746	
KXNet [6]		25.41	0.7675	27.14	0.7233	28.06	0.7674	31.16	0.8827	
KXNet-E <sub>X</sub>	<b>25.55</b>	<b>0.7709</b>	<b>27.19</b>	<b>0.7240</b>	<b>28.11</b>	<b>0.7679</b>	<b>31.20</b>	<b>0.8827</b>		
Bicubic	x2	22.19	0.5159	24.44	0.5150	24.38	0.5497	25.72	0.6241	15
RCAN [69]		21.28	0.3884	22.98	0.3822	22.96	0.4155	23.76	0.4706	
IKC [70]		24.69	0.7208	26.49	0.6828	26.93	0.7244	29.21	0.8260	
DASR [71]		24.84	0.7273	26.63	0.6841	27.22	0.7283	29.44	0.8322	
DAN [72]		25.32	0.7447	26.84	0.6932	27.56	0.7392	29.91	0.8430	
KXNet [6]		25.45	0.7492	26.87	0.6943	27.61	0.7409	29.95	0.8437	
KXNet-E <sub>X</sub>	<b>25.62</b>	<b>0.7578</b>	<b>26.91</b>	<b>0.6980</b>	<b>27.69</b>	<b>0.7435</b>	<b>30.00</b>	<b>0.8452</b>		
Bicubic	x3	21.18	0.4891	23.55	0.4961	23.28	0.5289	24.42	0.6119	15
RCAN [69]		20.22	0.3693	22.20	0.3726	21.99	0.4053	22.85	0.4745	
IKC [70]		24.21	0.7019	25.93	0.6564	26.42	0.7018	28.61	0.8135	
DASR [71]		23.93	0.6890	25.82	0.6484	26.27	0.6940	28.27	0.8047	
DAN [72]		24.17	0.7013	25.93	0.6551	26.46	0.7014	28.52	0.8130	
KXNet [6]		24.42	0.7117	26.00	0.6574	26.60	0.7054	28.69	0.8162	
KXNet-E <sub>X</sub>	<b>24.53</b>	<b>0.7181</b>	<b>26.03</b>	<b>0.6595</b>	<b>26.62</b>	<b>0.7074</b>	<b>28.75</b>	<b>0.8191</b>		
Bicubic	x4	20.38	0.4690	22.83	0.4841	22.39	0.5120	23.33	0.5977	15
RCAN [69]		19.23	0.3515	21.47	0.3686	21.05	0.3960	21.77	0.4689	
IKC [70]		23.35	0.6665	25.21	0.6238	25.58	0.6712	27.45	0.7867	
DASR [71]		23.26	0.6620	25.20	0.6223	25.55	0.6683	27.32	0.7842	
DAN [72]		23.48	0.6742	25.25	0.6283	25.72	0.6760	27.55	0.7938	
KXNet [6]		23.70	0.6842	25.30	0.6293	25.82	0.6790	27.71	0.7979	
KXNet-E <sub>X</sub>	<b>23.84</b>	<b>0.6895</b>	<b>25.34</b>	<b>0.6306</b>	<b>25.88</b>	<b>0.6805</b>	<b>27.79</b>	<b>0.7996</b>		



Fig. 5. Performance comparison on *img\_004* in Urban100 [62]. The scale factor is 4 and the standard deviation is 5.

Estimating  $X$  and  $K$  from  $Y$  constitutes a challenging ill-posed inverse problem. Nevertheless, the individual sub-problems pertaining to the estimation of  $X$  and  $K$  can be classified as instances of the broader inverse problem (2). By iteratively adapting the proximal gradient descent algorithm and deep unfolding technique for solving  $K$  and  $X$ , in a manner similar to Eqs. (3)-(5), [6] proposed the SOTA deep unfolding network, namely, KXNet. Specifically, the update formula for  $K$  is

$$K^{(t+1)} = \text{prox}_{\theta_K^{(t)}} \left( K^{(t)} - \delta_1 \nabla f \left( K^{(t)} \right) \right), \quad (12)$$

where  $\text{prox}_{\theta_K^{(t)}}(\cdot)$  is a shallow ResNet with the param-

eters  $\theta_K^{(t)}$ . Due to space limit, we don't represent the specific form of  $\nabla f(K^{(t-1)})$  here, which can be referred to [6]. Besides, the update formula for  $X$  is:

$$X^{(t+1)} = \text{prox}_{\theta_X^{(t)}} \left( X^{(t)} - \delta_2 K^{(t+1)} \otimes_s^T \left( Y - \left( X^{(t)} \otimes K^{(t+1)} \right) \downarrow_s \right) \right), \quad (13)$$

where  $\text{prox}_{\theta_X^{(t)}}(\cdot)$  is a shallow ResNet with the parameters  $\theta_X^{(t)}$ , and  $\otimes_s^T$  denotes the transposed convolution operation with stride as  $s$ .

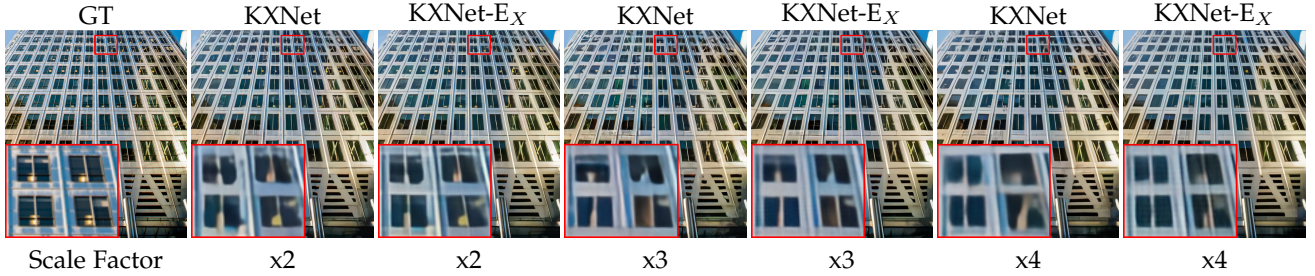
In KXNet,  $\text{prox}_{\theta_K^{(t)}}(\cdot)$  and  $\text{prox}_{\theta_X^{(t)}}(\cdot)$  are two important parts. The original KXNet employs a standard



TABLE 4

Generalization results of all comparison methods averaged on 50 standard deviation, while the model is trained with 0-25 standard deviation.

Method	Scale	Urban100 [62]		BSD100 [63]		Set14 [64]		Set5 [65]	
		PSNR	SSIM	PSNR	SSIM	PSNR	SSIM	PSNR	SSIM
KXNet	x2	23.27	0.6586	24.80	0.6071	25.14	0.6532	26.62	0.7652
KXNet-E <sub>X</sub>		<b>23.40</b>	<b>0.6653</b>	<b>24.84</b>	<b>0.6079</b>	<b>25.18</b>	<b>0.6541</b>	<b>26.66</b>	<b>0.7678</b>
KXNet	x3	22.28	0.6162	23.86	0.5742	24.08	0.6172	25.23	0.7229
KXNet-E <sub>X</sub>		<b>22.54</b>	<b>0.6307</b>	<b>24.06</b>	<b>0.5782</b>	<b>24.26</b>	<b>0.6229</b>	<b>25.43</b>	<b>0.7330</b>
KXNet	x4	21.83	0.5978	23.34	0.5532	23.45	0.5954	24.42	0.7047
KXNet-E <sub>X</sub>		<b>21.99</b>	<b>0.6064</b>	<b>23.49</b>	<b>0.5575</b>	<b>23.58</b>	<b>0.5999</b>	<b>24.55</b>	<b>0.7094</b>

Fig. 6. Performance comparison on *img 030* in Urban100 [62]. The standard deviation is 50.

CNN-based proximal network, which neglects the rotation symmetry prior in  $X$ . We thus exploit rotation equivariant convolution, F-Conv [57], and construct rotation equivariant proximal network for updating  $X$  in KXNet. The correlated method is denoted as KXNet-E<sub>X</sub> in the following.

**Network architecture Setting.** The structure of the equivariant proximal network is consistent with the  $\text{proxNet}_{\theta^{(t)}}(\cdot)$  structure in KXNet. It consists of a residual in residual (RIR) [73], which contains four residual blocks. We set  $t = 4$  for the equivariant convolutions, and the channel number of each residual block is reduced to  $1/4$  of the original networks in each layer to keep memory usage similar to the original network. Furthermore, the  $3 \times 3$  size filter in the original network is replaced with the  $5 \times 5$  filter in F-Conv to maintain the number of parameters. Before the global skip connection, a layer of  $3 \times 3$  CNN was added. The training settings and loss function follow the original settings. All the network parameters can be automatically learned from training data in an end-to-end manner.

**Datasets and Training settings.** Following [6], we use 3450 training images from DIV2K [66] and Flickr2K [74] datasets. For testing, we adopt commonly-used benchmark datasets, including Set5 [65], Set14 [64], BSD100 [63] and Urban100 [62]. We conduct experiments with anisotropic Gaussian blur kernel and Gaussian noise. For the training set, we set the kernel size  $p$  as 11/15/21 for  $\times 2/3/4$  SR, respectively. The kernel width at each axis is obtained by randomly rotating the widths  $\lambda_1$  and  $\lambda_2$  with an angle  $\theta \sim U[-\pi, \pi]$ , where  $\lambda_1$  and  $\lambda_2$  are uniformly distributed in  $U(0.6, 5.0)$ . Besides, the range of standard deviation  $\sigma$  for Gaussian noise is set as  $[0, 25]$ . For the testing datasets, we separately set the kernel width as  $\lambda_1 = 0.8, \lambda_2 = 1.6$  and  $\lambda_1 = 2.0, \lambda_2 = 4.0$ , and rotate them by  $\theta \in \{0, \pi/4, \pi/2, 3\pi/4\}$ , respectively. This means every HR testing image is degraded by 8 different blur kernels.

**Quantitative and qualitative comparison** As shown in Table 3, the proposed KXNet-E<sub>X</sub> consistently demonstrates

superior performance compared to other competing methods across four benchmark datasets encompassing varying SR scales and standard deviations. Fig. 5 visually shows the SR results of all competing methods on one typical sample. The proposed method clearly yields better restoration results, particularly in regions containing recurrent rotation-invariant structures within the image.

**Generalization performance.** To verify the generalization capability of the rotation equivariant proximal network, we further test the competing methods in new scenarios different from the training set. In Table. 4, we evaluate the comparison methods with AWGN whose standard deviation is 50, whereas the standard deviation in the training set ranges from 0 to 25. It can be observed that the image reconstruction accuracy of the proposed method significantly outperforms the competing method. Fig. 6 is the corresponding visualization result. The superiority of the rotation equivariant amelioration is also evident.

## 4.2 Metal Artifact Reduction in CT Image

During the computed tomography (CT) imaging process, metallic implants within patients would severely attenuate X-ray and even lead to missing X-ray projections. Accordingly, the captured CT images often present streaking and shading artifacts [75] [76], which negatively affect the clinical treatment. Therefore, the task of metal artifact reduction (MAR) in CT images has received extensive attention in the medical imaging field.

Normally, an observed metal-affected CT image consists of two parts, i.e. metal-free part and metal artifact part, as illustrated in Fig. 7. In the SOTA method [7] for metal artifacts removing, the degradation model for a metal-corrupted CT image  $Y \in \mathbb{R}^{H \times W}$ , is modeled as the following expression:

$$I \odot Y = I \odot X + I \odot M \quad (14)$$

where  $X, M \in \mathbb{R}^{H \times W}$  are the to-be-estimated clean metal-free CT image and the metal artifact layer, respectively,  $I \in$

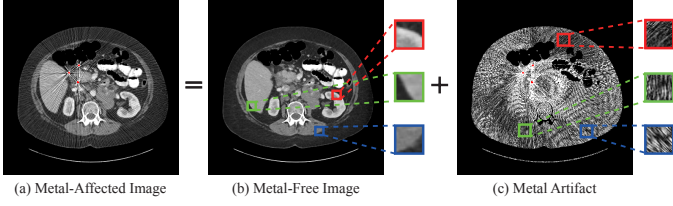


Fig. 7. (a) A metal-affected CT image of human tissue structures. (b) The metal-free part contains rotation symmetry visual patterns. (c) The metal artifacts part contains rotationally symmetrical streaking prior structures.

$\mathbb{R}^{H \times W}$  is a binary mask representing the non-metal region, and  $\odot$  is the point-wise multiplication operation.

Combining the model (14) with different metal artifact models, multiple algorithms and unfolding networks for metal artifact removal have been proposed. In the following, we adopt the suggested rotation equivariant proximal network into three SOTA unfolding networks for the task.

**Convolutional dictionary network for MAR.** Wang et al. proposed DICDNet [7], introducing a convolution dictionary mechanism to encode the structural prior knowledge of metal artifact layer  $M$ ,

$$M = \sum_{n=1}^N K_n \otimes M_n = \mathcal{K} \otimes \mathcal{M}, \quad (15)$$

where  $K_n \in \mathbb{R}^{f \times f}$  is a convolutional kernel with size  $f \times f$ , denoting the local patterns of artifacts, and  $M_n \in \mathbb{R}^{H \times W}$  is the corresponding feature map denoting the locations where local patterns appear,  $N$  is the number of kernels and  $\otimes$  is the 2D convolutional operation. For convenience, convolution and summation are further written in tensor form, i.e.  $\mathcal{K} \otimes \mathcal{M}$ .

By substituting (15) into (14), the subproblems for estimating  $\mathcal{M}$  and  $X$  are instances of the general inverse problem (2). Then by manners similar as Eqs. (3)-(5), DICDNet [7] got the network iterative structure of  $\mathcal{M}$  and  $X$  as:

$$\begin{cases} \mathcal{M}^{(t)} = \text{prox}_{\theta_{\mathcal{M}}^{(t)}}(\mathcal{M}^{(t-1)} - \eta_1 \nabla g_1(\mathcal{M}^{(t-1)})), \\ X^{(t)} = \text{prox}_{\theta_X^{(t)}}(X^{(t-1)} - \eta_2 \nabla g_2(X^{(t-1)})), \end{cases} \quad (16)$$

where  $\nabla g_1(\mathcal{M}^{(t-1)}) = \mathcal{K} \otimes^T (I \odot (\mathcal{K} \otimes \mathcal{M}^{(s-1)} + X^{(s-1)} - Y))$ ,  $\nabla g_2(X^{(t-1)}) = I \odot (\mathcal{K} \otimes \mathcal{M}^{(n)} + X^{(t-1)} - Y)$ ,  $\otimes^T$  denotes the transposed convolution operation,  $\text{prox}_{\theta_{\mathcal{M}}^{(t)}}(\cdot)$  and  $\text{prox}_{\theta_X^{(t)}}(\cdot)$  are proximal operator networks consisting of a simple ResNet structure, respectively. Among these operations,  $\otimes^T$ ,  $\otimes$ ,  $\odot$  can be easily implemented in Pytorch.

**Orientation-shared convolution for MAR.** Since the acquisition process of CT images is generally performed in a rotationally scanning manner, metal artifacts generally exhibit scattered streak structures, i.e., rotationally symmetrical streaking (RSS) prior as shown in Fig. 7 (c). In order to encode such inherent RSS prior structures, OSCNet [77] proposed a convolutional dictionary model based on filter parameterization that shares convolution filters among different angles:

$$M = \sum_{l=1}^L \sum_{k=1}^K C_k(\theta_l) \otimes M_{lk} = \mathcal{C} \otimes \mathcal{M}, \quad (17)$$

where  $L$  is the number of rotation angles,  $\theta_l = 2\pi(l-1)/L$  is the  $l^{\text{th}}$  rotation angles,  $K$  is the number of convolution filters at each angle,  $C_k(\theta_l) \in \mathbb{R}^{p \times p}$  is the  $k^{\text{th}}$  parameterized filter at angle  $\theta_l$ , and it represents the streaking and rotated prior patterns of artifacts,  $M_{lk}$  is feature map marking the location of artifacts, and  $\mathcal{C} \in \mathbb{R}^{p \times p \times LK}$  and  $\mathcal{M} \in \mathbb{R}^{H \times W \times LK}$  are stacked by  $C_k(\theta_l)$  and  $M_{lk}$ , respectively.

Similar to (16), the following iteration updating formulas of  $X$  and  $\mathcal{M}$  for model (17) can be deduced as [77]:

$$\begin{cases} \mathcal{M}^{(t)} = \text{prox}_{\theta_{\mathcal{M}}^{(t)}}(\mathcal{M}^{(t-1)} - \eta_1 \nabla g_1(\mathcal{M}^{(t-1)})), \\ X^{(t)} = \text{prox}_{\theta_X^{(t)}}(X^{(t-1)} - \eta_2 \nabla g_2(X^{(t-1)})), \end{cases} \quad (18)$$

where  $\nabla g_1(\mathcal{M}^{(t-1)}) = \mathcal{C} \otimes^T (I \odot (\mathcal{C} \otimes \mathcal{M}^{(s-1)} + X^{(s-1)} - Y))$ ,  $\nabla g_2(X^{(t-1)}) = I \odot (\mathcal{C} \otimes \mathcal{M}^{(n)} + X^{(t-1)} - Y)$ ,  $\otimes^T$  denotes the transposed convolution operation,  $\text{prox}_{\theta_{\mathcal{M}}^{(t)}}(\cdot)$  and  $\text{prox}_{\theta_X^{(t)}}(\cdot)$  are proximal networks consisting of a simple ResNet structure, respectively.

**Adaptive Convolution Dictionary for MAR.** In order to bridge the domain gap between the real scenarios and training data, an adaptive dictionary learning method for MAR is proposed, namely ACDNet [84]. Specifically, a metal artifact map  $M$  is obtained through a weighted convolutional dictionary model,

$$M = \sum_{n=1}^N (\mathcal{D} * W_n) \otimes M_n = (\mathcal{D} * W) \otimes \mathcal{M}, \quad (19)$$

where  $\mathcal{D} \in \mathbb{R}^{p \times p \times d}$  is a sample-invariant dictionary representing common local patterns of metal artifacts in CT images,  $W_n \in \mathbb{R}^d$  denotes weighted coefficient, and  $\mathcal{D} * W \otimes \mathcal{M}$  denotes the tensor form for convenience.

Similar to (16) and (18), the network iteration process for  $W$ ,  $\mathcal{M}$  and  $X$  can be then deduced, which is with the following formulation [84]:

$$\begin{cases} W^{(t)} = \text{prox}_{\theta_W^{(t)}}(W^{(t-1)} - \eta_1 \nabla g_1(W^{(t-1)})) \\ \mathcal{M}^{(t)} = \text{prox}_{\theta_{\mathcal{M}}^{(t)}}(\mathcal{M}^{(t-1)} - \eta_2 \nabla g_2(\mathcal{M}^{(t-1)})) \\ X^{(t)} = \text{prox}_{\theta_X^{(t)}}(X^{(t-1)} - \eta_3 \nabla g_3(X^{(t-1)})), \end{cases} \quad (20)$$

where  $\nabla g_1(W^{(t-1)}) = \partial g_1(W^{(t-1)})/\partial W$ ,  $\nabla g_2(\mathcal{M}^{(t-1)}) = (\mathcal{D} * W^{(t)}) \otimes^T (I \odot ((\mathcal{D} * W^{(t)}) \otimes \mathcal{M}^{(t-1)} + X^{(t-1)} - Y))$ ,  $\nabla g_3(X^{(t-1)}) = I \odot ((\mathcal{D} * W^{(t)}) \otimes \mathcal{M}^{(t)} + X^{(t-1)} - Y)$ , and  $\otimes^T$  denotes transposed convolution operator. Further,  $\text{prox}_{\theta_W^{(t)}}$ ,  $\text{prox}_{\theta_{\mathcal{M}}^{(t)}}$  and  $\text{prox}_{\theta_X^{(t)}}$  are three proximal operator networks.

It is evident that both the human tissue structures and the metal artifacts inherently exhibit rotation symmetry prior, as visually demonstrated in Fig. 7. Therefore, it is rational to employ rotation equivariant proximal networks for the estimation of  $\mathcal{M}$  and  $X$  within the frameworks of DICDNet and OSCNet. Notably, within the ACDNet, our focus narrows down to the estimation of  $X$  due to its distinct structure. Specifically, we apply the rotation equivariant proximal network for the estimation of  $X$  in DICDNet, which is denoted as DICDNet- $E_X$ . Extending our configuration to  $\mathcal{M}$  estimation as well, it is denoted as DICDNet- $E_X E_{\mathcal{M}}$ . We use the same notation strategy for ACDNet- $E_X$ , OSCNet- $E_X$  and OSCNet- $E_X E_{\mathcal{M}}$ , ensuring clarity and coherence throughout.

TABLE 5  
Average PSNR/SSIM of different competing methods on synthesized DeepLesion [78].

Method	Large Metal		→	Medium Metal		→	Small Metal		Average
Input	24.12 / 0.6761	26.13 / 0.7471		27.75 / 0.7659	28.53 / 0.7964		28.78 / 0.8076	27.06 / 0.7586	
LI [79]	27.21 / 0.8920	28.31 / 0.9185		29.86 / 0.9464	30.40 / 0.9555		30.57 / 0.9608	29.27 / 0.9347	
NMAR [80]	27.66 / 0.9114	28.81 / 0.9373		29.69 / 0.9465	30.44 / 0.9591		30.79 / 0.9669	29.48 / 0.9442	
CNNMAR [81]	28.92 / 0.9433	29.89 / 0.9588		30.84 / 0.9706	31.11 / 0.9743		31.14 / 0.9752	30.38 / 0.9644	
DuDoNet [76]	29.87 / 0.9723	30.60 / 0.9786		31.46 / 0.9839	31.85 / 0.9858		31.91 / 0.9862	31.14 / 0.9814	
DSCMAR [82]	34.04 / 0.9343	33.10 / 0.9362		33.37 / 0.9384	32.75 / 0.9393		32.77 / 0.9395	33.21 / 0.9375	
InDuDoNet [83]	36.74 / 0.9742	39.32 / 0.9893		41.86 / 0.9944	44.47 / 0.9948		45.01 / 0.9958	41.48 / 0.9897	
ACDNet [7]	37.28 / 0.9845	39.60 / 0.9903		42.19 / 0.9943	44.03 / 0.9957		44.11 / 0.9961	41.44 / 0.9922	
ACDNet- $E_X$	38.61 / 0.9893	40.65 / 0.9930		42.73 / 0.9955	44.76 / 0.9967		44.57 / 0.9968	<b>42.26 / 0.9943</b>	
DICDNet [7]	38.08 / 0.9872	39.98 / 0.9916		42.64 / 0.9944	44.96 / 0.9955		45.55 / 0.9960	42.24 / 0.9930	
DICDNet- $E_X$	38.40 / 0.9884	40.16 / 0.9924		42.72 / 0.9950	45.39 / 0.9961		45.75 / 0.9965	<b>42.48 / 0.9937</b>	
DICDNet- $E_X E_M$	38.85 / 0.9892	40.11 / 0.9925		42.88 / 0.9952	45.55 / 0.9963		45.98 / 0.9966	<b>42.67 / 0.9940</b>	
OSNet [77]	38.01 / 0.9871	40.20 / 0.9918		42.79 / 0.9945	44.51 / 0.9951		45.55 / 0.9960	42.21 / 0.9929	
OSNet- $E_X$	38.60 / 0.9891	40.18 / 0.9926		42.71 / 0.9951	44.99 / 0.9959		45.54 / 0.9965	<b>42.40 / 0.9938</b>	
OSNet- $E_X E_M$	39.16 / 0.9897	40.32 / 0.9929		43.28 / 0.9955	45.83 / 0.9964		46.16 / 0.9968	<b>42.95 / 0.9943</b>	

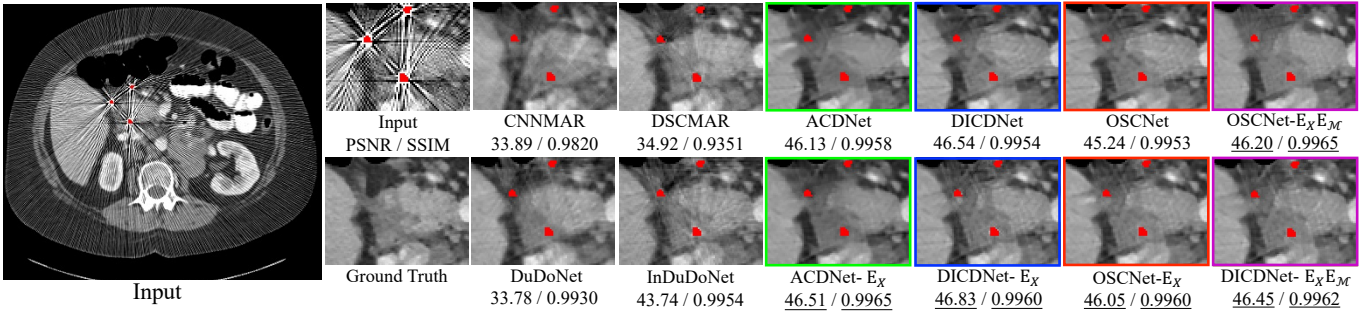


Fig. 8. Performance comparison on a typical metal-corrupted CT image from the synthesized DeepLesion [78]. The red pixels stand for metallic implants.

**Network architecture setting.** The rotation equivariant proximal network also adopts the residual structure, comprising four residual blocks. We exploit the  $p8$  group for the equivariant convolutions and set the channel number of each residual block to  $1/8$  of the original networks in each layer to maintain their similar memory usage. In addition, the  $3 \times 3$  size filter in the original network is replaced with the  $5 \times 5$  filter in F-Conv to preserve the number of parameters. And all the training settings and loss function are set the same as the original methods for fair competition.

**Datasets and Training Settings.** Following the synthetic procedure in [7], [77], we can generate the paired  $X$  and  $Y$  for training and testing by using 1,200 clean CT images from DeepLesion [78] and 100 simulated metallic implants from [81]. Consistent with the original work, we randomly select 90 masks and 1000 clean CT images to synthesize metal-corrupted training samples. The remaining 10 masks and 200 clean CT images are used to generate test samples. For training, except that the total epoch of DICDNet is changed to 200 to ensure convergence, all methods of replacing the rotation equivariant proximal network remain consistent with the original method.

**Quantitative and Qualitative Comparison.** As illustrated in Table 5, it is evident that when replacing the proximal networks of  $X$  and  $M$  in DICDNet with equivariant ameliorations, i.e., DICDNet- $E_X E_M$ , it is seen that the performance is significantly enhanced. Likewise, ACDNet- $E_X$  also enhances the recovery performance by replacing

the proximal network of the  $X$  subproblem in ACDNet. Moreover, OSCNet- $E_X$  replaces the proximal network for the  $X$  subproblem, also resulting in improved performance. Further, OSCNet- $E_X E_M$  considers the  $M$  subproblem, leading to even better results. Visually, as demonstrated in Fig. 8, the method with the replaced rotation equivariant proximal network performs better than the original method in removing metal artifacts and restoring the contour of human tissue structures. Both quantitative and qualitative comparisons reveal the superiority of the rotation equivariant embedded network over the original one.

**Generalization Results.** In order to show the generalization advantage of the rotation equivariant embedded method, we utilize another public dataset, CLINIC-metal [85], for testing. As shown in Fig. 9, the rotation equivariant proximal methods outperform the original results in terms of shadings and streaking artifacts removal, and they more accurately recover the human tissue structures. This provides an intuitive demonstration of the improved generalization ability of the ameliorated method.

### 4.3 Single Image Rain Removal

Images captured in rainy scenes suffer from unfavorable visual degradation, which increases the difficulty of many outdoor computer vision tasks, such as automatic driving and video surveillance. Therefore, rain removal from images is a meaningful research problem. Recently, Wang et al. designed a deep unfolding model, RCDNet [8], for rain

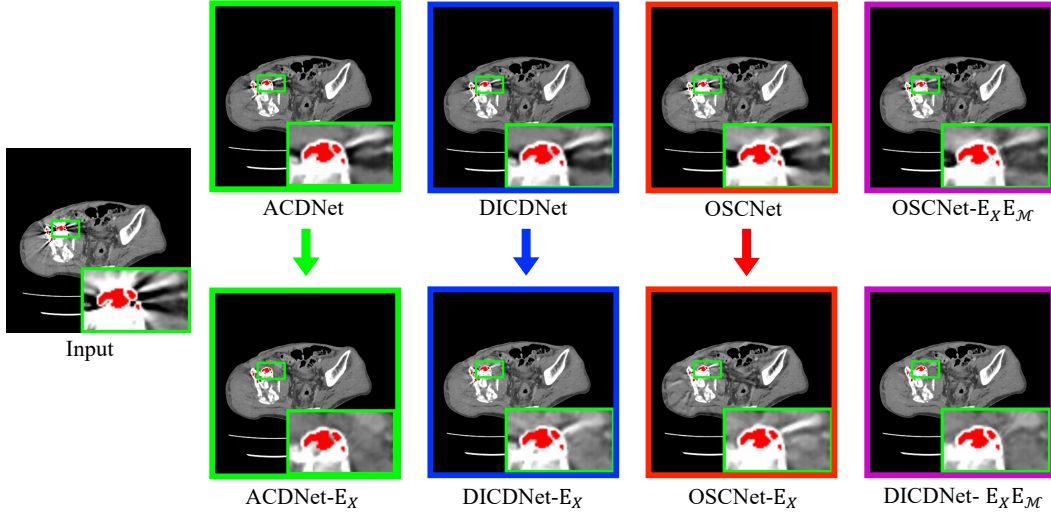


Fig. 9. Generalization results on a real clinical metal-affected CT image from CLINIC-metal [85]. The red pixels stand for metallic implants, which are segmented with the thresholding of 2500 HU.

TABLE 6  
Average PSNR/SSIM of different competing methods on four benchmark datasets.

Method	Rain100L [86]		Rain100H [86]		Rain1400 [87]		Rain12 [88]	
	PSNR	SSIM	PSNR	SSIM	PSNR	SSIM	PSNR	SSIM
Input	26.90	0.8384	13.56	0.3709	25.24	0.8097	30.14	0.8555
DSC [89]	27.34	0.8494	13.77	0.3199	27.88	0.8394	30.07	0.8664
GMM [88]	29.05	0.8717	15.23	0.4498	27.78	0.8585	32.14	0.9145
JCAS [90]	28.54	0.8524	14.62	0.4510	26.20	0.8471	33.10	0.9305
Clear [91]	30.24	0.9344	15.33	0.7421	26.21	0.8951	31.24	0.9353
DDN [87]	32.38	0.9258	22.85	0.7250	28.45	0.8888	34.04	0.9330
RESCAN [92]	38.52	0.9812	29.62	0.8720	32.03	0.9314	36.43	0.9519
PReNet [93]	37.45	0.9790	30.11	0.9053	32.55	0.9459	36.66	0.9610
SPANet [94]	35.33	0.9694	25.11	0.8332	29.85	0.9148	35.85	0.9572
JORDER_E [86]	38.59	0.9834	30.50	0.8967	32.00	0.9347	36.69	0.9621
SIRR [95]	32.37	0.9258	22.47	0.7164	28.44	0.8893	34.02	0.9347
RCDNet [8]	40.00	0.9860	31.28	0.9093	33.04	0.9472	37.61	<b>0.9644</b>
RCDNet-E <sub>B</sub>	<b>40.28</b>	<b>0.9867</b>	<b>31.43</b>	<b>0.9108</b>	<b>33.22</b>	<b>0.9488</b>	<b>37.66</b>	0.9617

removal based on a convolutional dictionary model and achieved SOTA performance. Normally, the observed color rainy image is denoted as  $\mathcal{O} \in \mathbb{R}^{H \times W \times 3}$ , which can be regarded as composed of the clean background image and the rain layer, expressed as follows:

$$\mathcal{O} = \mathcal{B} + \mathcal{R} = \mathcal{B} + \sum_{n=1}^N \mathcal{C}_n \otimes M_n, \quad (21)$$

where  $\mathcal{B}$  and  $\mathcal{R}$  denote the background and the rain layers, respectively,  $\mathcal{C}_n$  represents convolutional dictionary terms and  $M_n$  represents the corresponding rain feature map.

RCDNet exploits the proximal gradient descent algorithm and its unfolding network to estimate rain maps  $\mathcal{M}_n$  and rain-free background  $\mathcal{B}$ , simultaneously. It can also be classified as instances of the broader inverse problem (2). For solving  $\mathcal{M}$  and  $\mathcal{B}$ , by manners similar to Eqs. (3)-(5), the constructed network structures as follows:

$$\begin{cases} \mathcal{M}^{(t)} = \text{prox}_{\theta_{\mathcal{M}}^{(t)}}(\mathcal{M}^{(t-1)} - \eta_1 \nabla g_1(\mathcal{M}^{(t-1)})) \\ \mathcal{B}^{(t)} = \text{prox}_{\theta_{\mathcal{B}}^{(t)}}(\mathcal{B}^{(t-1)} - \eta_2 \nabla g_2(\mathcal{B}^{(t-1)})) \end{cases} \quad (22)$$

where  $\nabla g_1(\mathcal{M}^{(t-1)}) = \mathcal{C} \otimes^T (\sum_{n=1}^N \mathcal{C}_n \otimes M_n^{(t-1)} + \mathcal{B}^{(t-1)} - \mathcal{O})$ ,  $\nabla g_2(\mathcal{B}^{(t-1)}) = \sum_{n=1}^N \mathcal{C}_n \otimes M_n^{(t)} + \mathcal{B}^{(t-1)} - \mathcal{O}$ ,  $\mathcal{C} \in \mathbb{R}^{k \times k \times N \times 3}$  is a 4-dimensional tensor stacked by  $\mathcal{C}_n, n = 1, 2, \dots, N$ ;  $\otimes^T$  denotes the transposed convolution,  $\text{prox}_{\theta_{\mathcal{M}}^{(t)}}(\cdot)$  and  $\text{prox}_{\theta_{\mathcal{B}}^{(t)}}(\cdot)$  are two proximal networks consisting of a series of residual blocks, respectively. All network parameters can be learned in an end-to-end manner.

Since rain-free images have rich rotation-invariant structures and textures, the restored background image should maintain this structure prior even after rain streak removal. Therefore, it is rational to construct a rotation equivariant proximal network for  $\mathcal{B}$ . The correlated method is named RCDNet-E<sub>B</sub> in the following.

**Network architecture setting.** The equivariant proximal network also adopts the residual structure, which involves four residual blocks. We exploit the  $p8$  group for the equivariant convolutions and set the channel number of each residual block as  $1/8$  to the original networks in each layer to keep their similar memory. The  $3 \times 3$  size filter in the original network is replaced with the  $5 \times 5$  filter in F-Conv to preserve the number of parameters. All the training settings and loss function are set the same as the original RCDNet

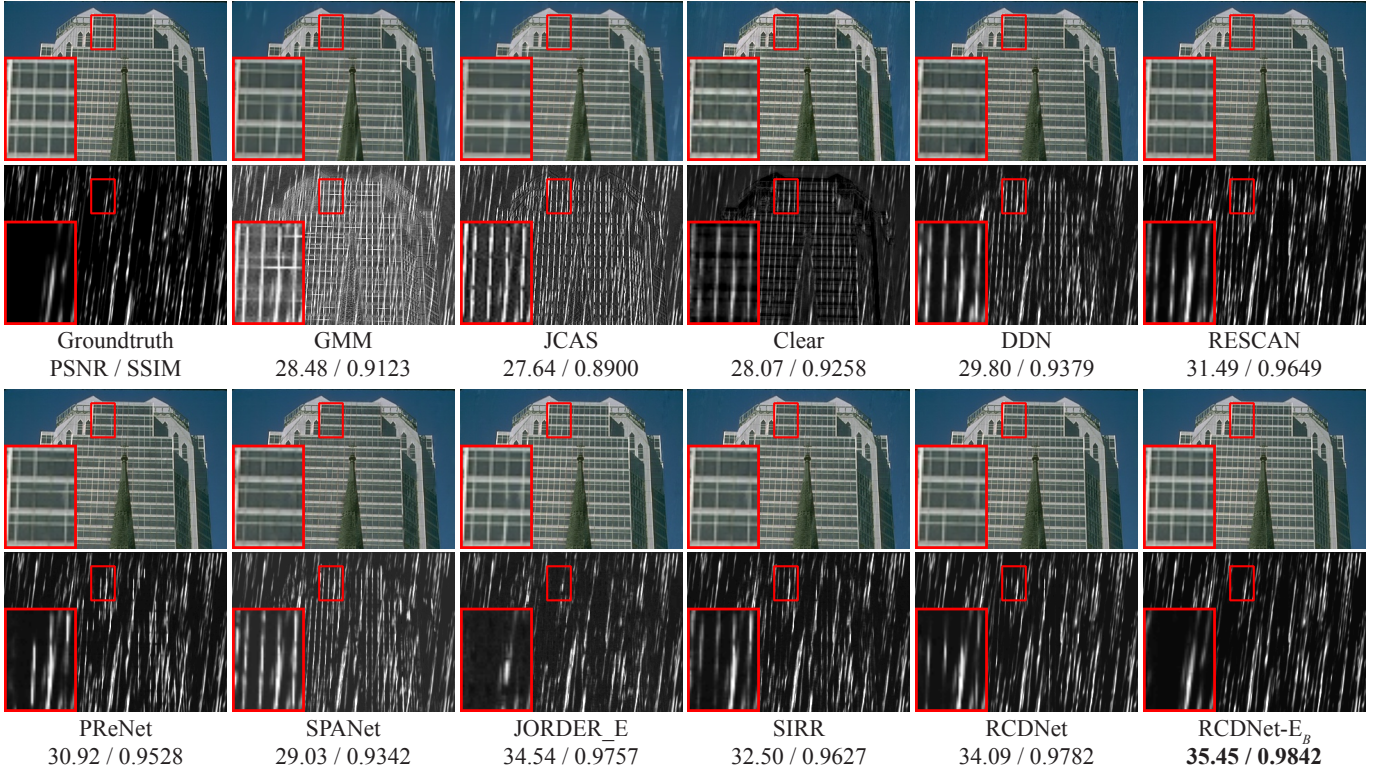


Fig. 10. The 1<sup>st</sup> column: a typical ground truth sample in Rain100L [86] dataset (upper) and its ground truth rain layer (lower). The 2<sup>nd</sup> – 12<sup>th</sup> columns: derained results (upper) and extracted rain layers (lower) by all competing methods

TABLE 7  
Average PSNR and SSIM comparisons on Dense10 [95] and Spare10 [95] of different deep models trained on Rain100H.

Datasets	Metrics	Input	DSC	JCAS	DDN	RESCAN	PReNet	SPANet	JORDER_E	SIRR	RCDNet	RCDNet-E <sub>B</sub>
Dense10	PSNR	19.17	20.85	19.93	21.38	21.81	21.91	20.28	21.66	21.23	21.89	<b>22.03</b>
	SSIM	0.8495	0.8811	0.8694	0.8965	0.9073	0.9236	0.8982	0.9093	0.8925	0.9239	<b>0.9248</b>
Spare10	PSNR	25.42	26.37	26.38	27.83	28.73	29.02	27.97	27.66	27.48	29.69	<b>29.75</b>
	SSIM	0.8956	0.8989	0.9043	0.9249	0.9337	0.9412	0.9279	0.9257	0.9181	0.9422	<b>0.9422</b>

for fair competition.

**Datasets and Training settings.** We compare our method with typical single image rain removal SOTA methods, including DSC [89], GMM [88], JCAS [90], Clear [91], DDN [87], RESCAN [92], PReNet [93], SPANet [94], JORDER\_E [86], SIRR [95], and RCDNet on four commonly-used benchmark datasets, i.e., Rain100L [86], Rain100H [86], Rain1400 [87], and Rain12 [88]. The training strategy is carried out according to the original settings, and the strategy of RCDNet-E<sub>B</sub> is the same as RCDNet.

**Quantitative and Qualitative Comparison.** As shown in Table 6, RCDNet-E<sub>B</sub> outperforms the other competing methods in both measures. Furthermore, as depicted in Fig. 10, our proposed method exhibits superior performance in removing visual rain streaks. It is worth noting that the model based on convolution sparse coding often mistakenly identifies white stripes as rain stripes, while RCDNet-E<sub>B</sub> configured with rotation equivariant proximal network can effectively alleviate this shortcoming. These results further support the effectiveness of adopting the rotation equivariant proximal network in this task.

**Generalization Results.** We then evaluate the proposed

method in the case that rain types are inconsistent between training and testing. We adopt Dense10 [95] and Sparse10 [95] to evaluate such generalization capability of all competing methods trained on Rain100H. From the quantitative results depicted in Table 7, it is seen that RCDNet-E<sub>B</sub> obtains higher PSNR and SSIM. This verifies that the proper embedding of rotation equivariance prior knowledge into the network is helpful to strengthen its generalization ability.

#### 4.4 Comparison of Number of Parameters

Additionally, we compared the number of parameters of the rotation equivariant proximal network to the standard CNN-based proximal network for the above methods and found that the former is more lightweight. Specifically, in blind single image super-resolution, we observed a parameter count of 5.50M for KXNet-E<sub>X</sub> versus 6.50M for KXNet. In metal artifact reduction in computed tomography, there are 1.27M for ACDNet-E<sub>X</sub> versus 1.60M for ACDNet, 0.72M for DICDNet-E<sub>X</sub>E<sub>M</sub> versus 1.28M for DICDNet and 0.72M for OSCNet-E<sub>X</sub>E<sub>M</sub> versus 1.28M for OSCNet. In single image rain removal, there is 2.40M for RCDNet-E<sub>B</sub> versus

3.17M for RCDNet. For more details, please refer to the supplementary material.

## 5 CONCLUSION

In this study, we have suggested a rotation equivariant proximal network based on F-Conv to alleviate the limitations of existing standard CNN-based proximal networks in capturing the rotation symmetry prior to images. Our approach embeds rotation symmetry priors into the deep unfolding framework via a rotation equivariant proximal network, leading to a more accurate representation of the image prior and improved model generalization ability. By leveraging the fact that the proximal network is rotation equivariant when the regularization term is invariant to rotation transformations, we have demonstrated the effectiveness of our proposed method in multiple typical low-level vision tasks, including blind image super-resolution, medical CT image reconstruction, and image de-raining, outperforming standard CNN-based proximal networks in capturing the rotation symmetry prior of images. Especially, we have first provided the theoretical equivariant error for such a designed proximal network with multi-layer networks under arbitrary rotation degrees, which should be the most refined theoretical conclusion for such error evaluation nowadays. This is specifically indispensable for supporting the rationale of this line of deep unfolding networks with intrinsic interpretability requirements and the potential usefulness of this methodology on more extensive image restoration tasks.

There is still large room for further enhancing the performance of the equivariant proximal operators. Firstly, proximal operators with more transformation equivariance are worth exploring, such as scale, affine, and color equivariance. Besides, equivariant modification for transformer-based proximal operators will also be explored in our future research. A more comprehensive and deep exploration of filter parametrization methods for designing high-accuracy equivariant convolution beyond F-Conv is also an important issue. Intuitively, bicubic/bilinear interpolation could be more suitable for filter parametrization in IR tasks, compared to the Fourier series expansion exploited in F-Conv.

## REFERENCES

- [1] Adrian Barbu. Training an active random field for real-time image denoising. *IEEE Transactions on Image Processing*, 18(11):2451–2462, 2009.
- [2] Kegan GG Samuel and Marshall F Tappen. Learning optimized map estimates in continuously-valued mrf models. In *2009 IEEE Conference on Computer Vision and Pattern Recognition*, pages 477–484. IEEE, 2009.
- [3] Jian Sun and Marshall F Tappen. Learning non-local range markov random field for image restoration. In *CVPR 2011*, pages 2745–2752. IEEE, 2011.
- [4] Yan Yang, Jian Sun, Huibin Li, and Zongben Xu. Deep admm-net for compressive sensing mri. In *Proceedings of the 30th International Conference on Neural Information Processing Systems*, pages 10–18, 2016.
- [5] Kai Zhang, Luc Van Gool, and Radu Timofte. Deep unfolding network for image super-resolution. In *Proceedings of the IEEE/CVF Conference on Computer Vision and Pattern Recognition*, pages 3217–3226, 2020.
- [6] Jiahong Fu, Hong Wang, Qi Xie, Qian Zhao, Deyu Meng, and Zongben Xu. Kxnet: A model-driven deep neural network for blind super-resolution. In *European Conference on Computer Vision*, pages 235–253. Springer, 2022.
- [7] Hong Wang, Yuexiang Li, Nanjun He, Kai Ma, Deyu Meng, and Yefeng Zheng. Dcdnet: Deep interpretable convolutional dictionary network for metal artifact reduction in ct images. *IEEE Transactions on Medical Imaging*, 41(4):869–880, 2021.
- [8] Hong Wang, Qi Xie, Qian Zhao, and Deyu Meng. A model-driven deep neural network for single image rain removal. In *Proceedings of the IEEE/CVF Conference on Computer Vision and Pattern Recognition*, pages 3103–3112, 2020.
- [9] Kaiming He, Xiangyu Zhang, Shaoqing Ren, and Jian Sun. Deep residual learning for image recognition. In *Proceedings of the IEEE Conference on Computer Vision and Pattern Recognition*, pages 770–778, 2016.
- [10] Qi Xie, Minghao Zhou, Qian Zhao, Zongben Xu, and Deyu Meng. Mhf-net: An interpretable deep network for multispectral and hyperspectral image fusion. *IEEE Transactions on Pattern Analysis and Machine Intelligence*, 2020.
- [11] Olaf Ronneberger, Philipp Fischer, and Thomas Brox. U-net: Convolutional networks for biomedical image segmentation. In *Medical Image Computing and Computer-Assisted Intervention–MICCAI 2015: 18th International Conference, Munich, Germany, October 5–9, 2015, Proceedings, Part III 18*, pages 234–241. Springer, 2015.
- [12] Kai Zhang, Wangmeng Zuo, Shuhang Gu, and Lei Zhang. Learning deep cnn denoiser prior for image restoration. In *Proceedings of the IEEE Conference on Computer Vision and Pattern Recognition*, pages 3929–3938, 2017.
- [13] Kai Zhang, Yawei Li, Wangmeng Zuo, Lei Zhang, Luc Van Gool, and Radu Timofte. Plug-and-play image restoration with deep denoiser prior. *IEEE Transactions on Pattern Analysis and Machine Intelligence*, 44(10):6360–6376, 2022.
- [14] Kai Zhang, Yawei Li, Jingyun Liang, Jiezhang Cao, Yulun Zhang, Hao Tang, Radu Timofte, and Luc Van Gool. Practical blind denoising via swin-conv-unet and data synthesis. *arXiv preprint arXiv:2203.13278*, 2022.
- [15] Elena Celledoni, Matthias J Ehrhardt, Christian Etmann, Brynjulf Owren, Carola-Bibiane Schönlieb, and Ferdia Sherry. Equivariant neural networks for inverse problems. *Inverse Problems*, 37(8):085006, 2021.
- [16] Lixin Shen, Manos Papadakis, Ioannis A Kakadiaris, Ioannis Konstantinidis, Donald Kouri, and David Hoffman. Image denoising using a tight frame. *IEEE Transactions on Image Processing*, 15(5):1254–1263, 2006.
- [17] Michael Elad. *Sparse and redundant representations: from theory to applications in signal and image processing*, volume 2. Springer, 2010.
- [18] Leonid I Rudin, Stanley Osher, and Emad Fatemi. Nonlinear total variation based noise removal algorithms. *Physica D: nonlinear phenomena*, 60(1–4):259–268, 1992.
- [19] Daniel Zoran and Yair Weiss. From learning models of natural image patches to whole image restoration. In *2011 International Conference on Computer Vision*, pages 479–486. IEEE, 2011.
- [20] Aram Danielyan, Vladimir Katkovnik, and Karen Egiazarian. Bm3d frames and variational image deblurring. *IEEE Transactions on image processing*, 21(4):1715–1728, 2011.
- [21] Felix Heide, Markus Steinberger, Yun-Ta Tsai, Mushfiqur Rouf, Dawid Pajak, Dikpal Reddy, Orazio Gallo, Jing Liu, Wolfgang Heidrich, Karen Egiazarian, et al. Flexisp: A flexible camera image processing framework. *ACM Transactions on Graphics (ToG)*, 33(6):1–13, 2014.
- [22] Singanallur V Venkatakrishnan, Charles A Bouman, and Brendt Wohlberg. Plug-and-play priors for model based reconstruction. In *2013 IEEE Global Conference on Signal and Information Processing*, pages 945–948. IEEE, 2013.
- [23] Arie Rond, Raja Giryes, and Michael Elad. Poisson inverse problems by the plug-and-play scheme. *Journal of Visual Communication and Image Representation*, 41:96–108, 2016.
- [24] Kostadin Dabov, Alessandro Foi, Vladimir Katkovnik, and Karen Egiazarian. Image denoising by sparse 3-d transform-domain collaborative filtering. *IEEE Transactions on image processing*, 16(8):2080–2095, 2007.
- [25] Tim Meinhardt, Michael Moller, Caner Hazirbas, and Daniel Cremers. Learning proximal operators: Using denoising networks for regularizing inverse imaging problems. In *Proceedings of the IEEE International Conference on Computer Vision*, pages 1781–1790, 2017.
- [26] JH Rick Chang, Chun-Liang Li, Barnabas Poczos, BVK Vijaya Kumar, and Aswin C Sankaranarayanan. One network to solve them all—solving linear inverse problems using deep projection models. In *Proceedings of the IEEE International Conference on Computer Vision*, pages 5888–5897, 2017.

- [27] Weisheng Dong, Peiyao Wang, Wotao Yin, Guangming Shi, Fangfang Wu, and Xiaotong Lu. Denoising prior driven deep neural network for image restoration. *IEEE Transactions on Pattern Analysis and Machine Intelligence*, 41(10):2305–2318, 2018.
- [28] Tom Tzirer and Raja Giryes. Image restoration by iterative denoising and backward projections. *IEEE Transactions on Image Processing*, 28(3):1220–1234, 2018.
- [29] Kai Zhang, Wangmeng Zuo, Yunjin Chen, Deyu Meng, and Lei Zhang. Beyond a gaussian denoiser: Residual learning of deep cnn for image denoising. *IEEE Transactions on Image Processing*, 26(7):3142–3155, 2017.
- [30] Ji He, Yan Yang, Yongbo Wang, Dong Zeng, Zhaoying Bian, Hao Zhang, Jian Sun, Zongben Xu, and Jianhua Ma. Optimizing a parameterized plug-and-play admm for iterative low-dose ct reconstruction. *IEEE Transactions on Medical Imaging*, 38(2):371–382, 2018.
- [31] Karol Gregor and Yann LeCun. Learning fast approximations of sparse coding. In *Proceedings of the 27th International Conference on International Conference on Machine Learning*, pages 399–406, 2010.
- [32] Manyà V Afonso, José M Bioucas-Dias, and Mário AT Figueiredo. Fast image recovery using variable splitting and constrained optimization. *IEEE Transactions on Image Processing*, 19(9):2345–2356, 2010.
- [33] Zhaowen Wang, Ding Liu, Jianchao Yang, Wei Han, and Thomas Huang. Deep networks for image super-resolution with sparse prior. In *Proceedings of the IEEE International Conference on Computer Vision*, pages 370–378, 2015.
- [34] Yunjin Chen and Thomas Pock. Trainable nonlinear reaction diffusion: A flexible framework for fast and effective image restoration. *IEEE Transactions on Pattern Analysis and Machine Intelligence*, 39(6):1256–1272, 2016.
- [35] Jonas Adler and Ozan Öktem. Solving ill-posed inverse problems using iterative deep neural networks. *Inverse Problems*, 33(12):124007, 2017.
- [36] Patrick Putzky and Max Welling. Recurrent inference machines for solving inverse problems. *arXiv preprint arXiv:1706.04008*, 2017.
- [37] Pablo Sprechmann, Roee Litman, Tal Ben Yakar, Alexander M Bronstein, and Guillermo Sapiro. Supervised sparse analysis and synthesis operators. *Advances in Neural Information Processing Systems*, 26, 2013.
- [38] Xuehan Xiong and Fernando De la Torre. Supervised descent method and its applications to face alignment. In *Proceedings of the IEEE Conference on Computer Vision and Pattern Recognition*, pages 532–539, 2013.
- [39] Maojia Li, Jialin Liu, and Wotao Yin. Learning to combine quasi-newton methods.
- [40] Dong Yang and Jian Sun. Proximal dehaze-net: A prior learning-based deep network for single image dehazing. In *Proceedings of the European Conference on Computer Vision (ECCV)*, pages 702–717, 2018.
- [41] Thomas Blumensath and Mike E Davies. Iterative thresholding for sparse approximations. *Journal of Fourier Analysis and Applications*, 14(5):629–654, 2008.
- [42] Amir Beck and Marc Teboulle. A fast iterative shrinkage-thresholding algorithm for linear inverse problems. *SIAM Journal on Imaging Sciences*, 2(1):183–202, 2009.
- [43] Thomas Moreau and Joan Bruna. Understanding the learned iterative soft thresholding algorithm with matrix factorization. *arXiv preprint arXiv:1706.01338*, 2017.
- [44] Aviad Aberdam, Alona Golts, and Michael Elad. Ada-lista: Learned solvers adaptive to varying models. *IEEE Transactions on Pattern Analysis and Machine Intelligence*, 2021.
- [45] Jialin Liu and Xiaohan Chen. Alista: Analytic weights are as good as learned weights in lista. In *International Conference on Learning Representations (ICLR)*, 2019.
- [46] Raied Aljadaany, Dipan K Pal, and Marios Savvides. Proximal splitting networks for image restoration. In *International Conference on Image Analysis and Recognition*, pages 3–17. Springer, 2019.
- [47] Jonas Adler and Ozan Öktem. Learned primal-dual reconstruction. *IEEE Transactions on Medical Imaging*, 37(6):1322–1332, 2018.
- [48] Taco Cohen and Max Welling. Group equivariant convolutional networks. In *International Conference on Machine Learning*, pages 2990–2999. PMLR, 2016.
- [49] Emiel Hoogeboom, Jorn WT Peters, Taco S Cohen, and Max Welling. Hexaconv. In *International Conference on Learning Representations*, 2018.
- [50] Yanzhao Zhou, Qixiang Ye, Qiang Qiu, and Jianbin Jiao. Oriented response networks. In *Proceedings of the IEEE Conference on Computer Vision and Pattern Recognition*, pages 519–528, 2017.
- [51] Diego Marcos, Michele Volpi, Nikos Komodakis, and Devis Tuia. Rotation equivariant vector field networks. In *Proceedings of the IEEE International Conference on Computer Vision*, pages 5048–5057, 2017.
- [52] Daniel E Worrall, Stephan J Garbin, Daniyar Turmukhambetov, and Gabriel J Brostow. Harmonic networks: Deep translation and rotation equivariance. In *Proceedings of the IEEE Conference on Computer Vision and Pattern Recognition*, pages 5028–5037, 2017.
- [53] Maurice Weiler, Fred A Hamprecht, and Martin Storath. Learning steerable filters for rotation equivariant cnns. In *Proceedings of the IEEE Conference on Computer Vision and Pattern Recognition*, pages 849–858, 2018.
- [54] Maurice Weiler and Gabriele Cesa. General e(2)-equivariant steerable cnns. *Advances in Neural Information Processing Systems*, 32, 2019.
- [55] Zhengyang Shen, Lingshen He, Zhouchen Lin, and Jinwen Ma. Pdo-econv: Partial differential operator based equivariant convolutions. In *International Conference on Machine Learning*, pages 8697–8706. PMLR, 2020.
- [56] Zhengyang Shen, Tiancheng Shen, Zhouchen Lin, and Jinwen Ma. Pdo-es2cnns: Partial differential operator based equivariant spherical cnns. In *Proceedings of the AAAI Conference on Artificial Intelligence*, volume 35, pages 9585–9593, 2021.
- [57] Qi Xie, Qian Zhao, Zongben Xu, and Deyu Meng. Fourier series expansion based filter parametrization for equivariant convolutions. *IEEE Transactions on Pattern Analysis and Machine Intelligence*, 2022.
- [58] Heinz Werner Engl, Martin Hanke, and Andreas Neubauer. *Regularization of inverse problems*, volume 375. Springer Science & Business Media, 1996.
- [59] David L Donoho. De-noising by soft-thresholding. *IEEE Transactions on Information Theory*, 41(3):613–627, 1995.
- [60] Jean Jacques Moreau. Fonctions convexes duales et points proximaux dans un espace hilbertien. *Comptes rendus hebdomadaires des séances de l’Académie des sciences*, 255:2897–2899, 1962.
- [61] Risi Kondor and Shubendu Trivedi. On the generalization of equivariance and convolution in neural networks to the action of compact groups. In *International Conference on Machine Learning*, pages 2747–2755. PMLR, 2018.
- [62] Jia-Bin Huang, Abhishek Singh, and Narendra Ahuja. Single image super-resolution from transformed self-exemplars. In *Proceedings of the IEEE Conference on Computer Vision and Pattern Recognition*, pages 5197–5206, 2015.
- [63] David Martin, Charless Fowlkes, Doron Tal, and Jitendra Malik. A database of human segmented natural images and its application to evaluating segmentation algorithms and measuring ecological statistics. In *Proceedings Eighth IEEE International Conference on Computer Vision. ICCV 2001*, volume 2, pages 416–423. IEEE, 2001.
- [64] Roman Zeyde, Michael Elad, and Matan Protter. On single image scale-up using sparse-representations. In *International Conference on Curves and Surfaces*, pages 711–730. Springer, 2010.
- [65] Marco Bevilacqua, Aline Roumy, Christine Guillemot, and Marie Line Alberi-Morel. Low-complexity single-image super-resolution based on nonnegative neighbor embedding. 2012.
- [66] Eirikur Agustsson and Radu Timofte. Ntire 2017 challenge on single image super-resolution: Dataset and study. In *Proceedings of the IEEE conference on computer vision and pattern recognition workshops*, pages 126–135, 2017.
- [67] Xavier Glorot and Yoshua Bengio. Understanding the difficulty of training deep feedforward neural networks. In *Proceedings of the Thirteenth International Conference on Artificial Intelligence and Statistics*, pages 249–256, 2010.
- [68] Kaiming He, Xiangyu Zhang, Shaoqing Ren, and Jian Sun. Delving deep into rectifiers: Surpassing human-level performance on imagenet classification. In *Proceedings of the IEEE International Conference on Computer Vision (ICCV)*, December 2015.
- [69] Yulun Zhang, Kunpeng Li, Kai Li, Lichen Wang, Bineng Zhong, and Yun Fu. Image super-resolution using very deep residual channel attention networks. In *Proceedings of the European Conference on Computer Vision (ECCV)*, pages 286–301, 2018.
- [70] Jinjin Gu, Hannan Lu, Wangmeng Zuo, and Chao Dong. Blind super-resolution with iterative kernel correction. In *Proceedings of the IEEE/CVF Conference on Computer Vision and Pattern Recognition*, pages 1604–1613, 2019.

- [71] Longguang Wang, Yingqian Wang, Xiaoyu Dong, Qingyu Xu, Jungang Yang, Wei An, and Yulan Guo. Unsupervised degradation representation learning for blind super-resolution. In *Proceedings of the IEEE/CVF Conference on Computer Vision and Pattern Recognition*, pages 10581–10590, 2021.
- [72] Zhengxiong Luo, Yan Huang, Shang Li, Liang Wang, and Tieniu Tan. Unfolding the alternating optimization for blind super resolution. *arXiv preprint arXiv:2010.02631*, 2020.
- [73] Yulun Zhang, Kunpeng Li, Kai Li, Lichen Wang, Bineng Zhong, and Yun Fu. Image super-resolution using very deep residual channel attention networks. In *ECCV*, 2018.
- [74] Radu Timofte, Eirikur Agustsson, Luc Van Gool, Ming-Hsuan Yang, and Lei Zhang. Ntire 2017 challenge on single image super-resolution: Methods and results. In *Proceedings of the IEEE conference on Computer Vision and Pattern Recognition Workshops*, pages 114–125, 2017.
- [75] Haofu Liao, Wei-An Lin, S Kevin Zhou, and Jiebo Luo. Adn: artifact disentanglement network for unsupervised metal artifact reduction. *IEEE Transactions on Medical Imaging*, 39(3):634–643, 2019.
- [76] Wei-An Lin, Haofu Liao, Cheng Peng, Xiaohang Sun, Jingdan Zhang, Jiebo Luo, Rama Chellappa, and Shaohua Kevin Zhou. Dudonet: Dual domain network for ct metal artifact reduction. In *Proceedings of the IEEE/CVF Conference on Computer Vision and Pattern Recognition*, pages 10512–10521, 2019.
- [77] Hong Wang, Qi Xie, Yuexiang Li, Yawen Huang, Deyu Meng, and Yefeng Zheng. Orientation-shared convolution representation for ct metal artifact learning. In *International Conference on Medical Image Computing and Computer-Assisted Intervention*, pages 665–675. Springer, 2022.
- [78] Ke Yan, Xiaosong Wang, Le Lu, Ling Zhang, Adam P Harrison, Mohammadhadi Bagheri, and Ronald M Summers. Deep lesion graphs in the wild: relationship learning and organization of significant radiology image findings in a diverse large-scale lesion database. In *Proceedings of the IEEE Conference on Computer Vision and Pattern Recognition*, pages 9261–9270, 2018.
- [79] Willi A Kalender, Robert Hebel, and Johannes Ebersberger. Reduction of ct artifacts caused by metallic implants. *Radiology*, 164(2):576–577, 1987.
- [80] Esther Meyer, Rainer Raupach, Michael Lell, Bernhard Schmidt, and Marc Kachelrieß. Normalized metal artifact reduction (nmar) in computed tomography. *Medical physics*, 37(10):5482–5493, 2010.
- [81] Yanbo Zhang and Hengyong Yu. Convolutional neural network based metal artifact reduction in x-ray computed tomography. *IEEE Transactions on Medical Imaging*, 37(6):1370–1381, 2018.
- [82] Lequan Yu, Zhicheng Zhang, Xiaomeng Li, and Lei Xing. Deep sinogram completion with image prior for metal artifact reduction in ct images. *IEEE Transactions on Medical Imaging*, 40(1):228–238, 2020.
- [83] Hong Wang, Yuexiang Li, Haimiao Zhang, Jiawei Chen, Kai Ma, Deyu Meng, and Yefeng Zheng. Indudonet: an interpretable dual domain network for ct metal artifact reduction. In *Medical Image Computing and Computer Assisted Intervention—MICCAI 2021: 24th International Conference, Strasbourg, France, September 27–October 1, 2021, Proceedings, Part VI 24*, pages 107–118. Springer, 2021.
- [84] Hong Wang, Yuexiang Li, Deyu Meng, and Yefeng Zheng. Adaptive convolutional dictionary network for ct metal artifact reduction. *arXiv preprint arXiv:2205.07471*, 2022.
- [85] Pengbo Liu, Hu Han, Yuanqi Du, Heqin Zhu, Yin hao Li, Feng Gu, Honghu Xiao, Jun Li, Chunpeng Zhao, Li Xiao, et al. Deep learning to segment pelvic bones: large-scale ct datasets and baseline models. *International Journal of Computer Assisted Radiology and Surgery*, 16:749–756, 2021.
- [86] Wenhan Yang, Robby T Tan, Jiashi Feng, Zongming Guo, Shuicheng Yan, and Jiaying Liu. Joint rain detection and removal from a single image with contextualized deep networks. *IEEE Transactions on Pattern Analysis and Machine Intelligence*, 42(6):1377–1393, 2019.
- [87] Xueyang Fu, Jiabin Huang, Delu Zeng, Yue Huang, Xinghao Ding, and John Paisley. Removing rain from single images via a deep detail network. In *Proceedings of the IEEE Conference on Computer Vision and Pattern Recognition*, pages 3855–3863, 2017.
- [88] Yu Li, Robby T Tan, Xiaojie Guo, Jiangbo Lu, and Michael S Brown. Rain streak removal using layer priors. In *Proceedings of the IEEE Conference on Computer Vision and Pattern Recognition*, pages 2736–2744, 2016.
- [89] Yu Luo, Yong Xu, and Hui Ji. Removing rain from a single image via discriminative sparse coding. In *Proceedings of the IEEE International Conference on Computer Vision*, pages 3397–3405, 2015.
- [90] Shuhang Gu, Deyu Meng, Wangmeng Zuo, and Lei Zhang. Joint convolutional analysis and synthesis sparse representation for single image layer separation. In *Proceedings of the IEEE International Conference on Computer Vision*, pages 1708–1716, 2017.
- [91] Xueyang Fu, Jiabin Huang, Xinghao Ding, Yinghao Liao, and John Paisley. Clearing the skies: A deep network architecture for single-image rain removal. *IEEE Transactions on Image Processing*, 26(6):2944–2956, 2017.
- [92] Xia Li, Jianlong Wu, Zhouchen Lin, Hong Liu, and Hongbin Zha. Recurrent squeeze-and-excitation context aggregation net for single image deraining. In *Proceedings of the European Conference on Computer Vision (ECCV)*, pages 254–269, 2018.
- [93] Dongwei Ren, Wangmeng Zuo, Qinghua Hu, Pengfei Zhu, and Deyu Meng. Progressive image deraining networks: A better and simpler baseline. In *Proceedings of the IEEE/CVF Conference on Computer Vision and Pattern Recognition*, pages 3937–3946, 2019.
- [94] Tianyu Wang, Xin Yang, Ke Xu, Shaozhe Chen, Qiang Zhang, and Rynson WH Lau. Spatial attentive single-image deraining with a high quality real rain dataset. In *Proceedings of the IEEE/CVF Conference on Computer Vision and Pattern Recognition*, pages 12270–12279, 2019.
- [95] Wei Wei, Deyu Meng, Qian Zhao, Zongben Xu, and Ying Wu. Semi-supervised transfer learning for image rain removal. In *Proceedings of the IEEE/CVF Conference on Computer Vision and Pattern Recognition*, pages 3877–3886, 2019.